Correction 1

Hydrothermal troctolite alteration at 300 and 400°C – Insights from flexible Au-reaction cell batch experimental investigations (Word Count: 9993)

Christian T. Hansen[a,b*], C. Johan Lissenberg[c], Wolf-Achim Kahl[a,d] and Wolfgang Bach[a,b]

[a] Geosciences Department, University of Bremen, Bremen, 28359, Germany

[b] MARUM Center for Marine Environmental Sciences, Bremen, 28359, Germany

[c] School of Earth and Ocean Sciences, Cardiff University, Cardiff CF10 3AT, United Kingdom

[d] MAPEX Center for Materials and Processes, University of Bremen, Bremen, Germany

Abstract

Troctolites are increasingly recognized as a common rock found in association with oceanic core complexes. They are similar to komatiite in composition and troctolite alteration hence may provide insight into H_2 production on Early Earth. We investigated the hydrothermal alteration of olivine-rich troctolites in two batch experiments (300 °C, 400 °C and 40 MPa) by reacting forsteritic olivine and anorthite-rich plagioclase with salt solutions. The alteration process was evaluated based on concomitant fluid samples and solids retrieved upon termination of the experiments. In both experiments the initial rock powder was turned into a hard, compact mass through cementation by secondary phases. The heterogeneity of this mass was documented using μ-computed tomography and electron microscopy. Thermodynamic computations were conducted to determine the equilibrium phase assemblages and fluid compositions with increasing reaction turnover. Mineral zonation developed between the fast reacting, fluid dominated top portion of the solids and the more isolated portions at the bottom of the reaction cell. At 300 °C, the total

reaction turnover after 1800 hrs was 77.5 %. Serpentinization of olivine controlled the fluid composition after plagioclase had reacted away in the top layers. In contrast, a Ca and Al-enriched assemblage of xonotlite and chlorite developed alongside unreacted plagioclase at the bottom. The porosity is very low in the top layers, but high (around 15%) in the bottom part of the cemented mass. At 400 °C, the reaction turnover was only 51% as olivine was stable after plagioclase had reacted away. Clinopyroxene, andradite ± chlorite had formed in the top layers, whereas xonotlite, grossular and chlorite had formed at the bottom. The permeability is more uniform and the mineral zonation less pronounced at 400 °C. These mineral zonations developed as a consequence of an increased mobility of Ca, Al, Mg and to a lesser extent of Fe in the experiment, which may be facilitated in the highly permeable granular materials when compared to a compact rock. Steady-state hydrogen concentrations were at least 20 mmol L^{-1} at 300 °C and <1 mmol L^{-1} at 400 °C. A lack of magnetite formation at the higher temperature is responsible for the low H_2 yields.

Keywords: Troctolite alteration, Experimental petrology/geochemistry, Hydrogen, Fluid-rock interaction

*Corresponding author: c.hansen@uni-bremen.de

INTRODUCTION

Oceanic core complexes (OCCs) are the result of extensive detachment faulting and exhumation along slow and ultraslow spreading ridges and provide a unique opportunity to study fluid-rock interactions between seawater and ultramafic lithologies (Blackman et al. 1998; Smith et al. 2008, 2012). These unique settings have attracted increasing interest, especially since hydrothermal systems hosted in OCCs produce some of the most

47 fascinating geochemical environments on earth (Charlou et al. 2002; Schmidt et al. 2007;
48 German et al. 2010). The hydrothermal fluids originating from alteration of ultramafic
49 rocks are often extremely enriched in H_2 and CH_4, which support chemolithoautotrophic
50 microorganisms in core complex-hosted hydrothermal vent systems (Takai et al. 2004;
51 Kelley et al., 2005). The production of H_2 and CH_4 in these systems is commonly related
52 to serpentinization of mantle peridotite (Charlou et al. 2002; Sleep et al. 2004; Takai et al.
53 2004; Proskurowski et al. 2006; Konn et al. 2015), and hence most studies investigating
54 the underlying reactions focused on ultramafic rocks (Seyfried et al. 2007; Klein et al.
55 2009, 2013; McCollom and Bach 2009; Cannat et al. 2010). However, other lithologies
56 associated with OCCs reveal a high geochemical diversity of rocks in the crust-mantle
57 transition zone facilitated by varied water-rock reactions during OCC exhumation such as
58 rodingitization (Bach and Klein 2008; Frost et al. 2008) or melt impregnation of mantle
59 peridotite (Jöns et al. 2010; Albers et al., 2019). These metasomatic reactions are driven by
60 strong contrasts in chemical potential between major rock components, such as silica (Frost
61 and Beard 2007; Klein et al. 2009, 2014). In this respect, troctolites provide an excellent
62 example where enhanced compositional contrasts between forsterite-rich olivine and calcic
63 plagioclase are key to the reactions observed during hydrothermal alteration (Frost et al.
64 2008). Troctolites are common in the lower crust and crust-mantle transition zone, and
65 were long believed to represent magmatic cumulates. The origin of troctolites may be
66 varied, however, and is subject to an ongoing discussion (Ildefonse et al. 2006; Dick et al.
67 2008; Suhr et al. 2008; Drouin et al. 2009, 2010; Blackman et al. 2011; Renna and Tribuzio
68 2011; Sanfilippo and Tribuzio 2013; Sanfilippo et al. 2013). Nakamura et al. (2009)
69 investigated altered olivine-rich troctolites near the Kairei hydrothermal vent field and

highlighted the potential of troctolite-seawater reactions for producing strong enrichments of H_2. In this context, Kumagai et al. (2008) emphasized the significance of this H_2 production pathway for the early emergence of life as the geochemical character of troctolites resembles that of komatiites.

However, only few studies investigated the alteration of troctolitic rocks (Frost et al. 2008; Beard et al. 2009; Nakamura et al. 2009; Nozaka et al. 2017; McCaig et al. 2018). Frost et al. (2008) suggested that the troctolite alteration resembles a one-rock rodingitization, in which olivine represents the ultramafic and plagioclase the gabbroic component. The observed mineral assemblages include serpentine, magnetite, and brucite associated with olivine as well as prehnite, hydrogrossular and clinozoisite associated with plagioclase. Frost et al. (2008) further proposed an alteration temperature of <350 °C for serpentinized troctolites from Atlantis Massif. Similarly, Bach and Klein (2008) suggested that rodingitization can only proceed if olivine reacts to serpentine and brucite at temperatures <350 °C. At higher temperatures, serpentinization of olivine and rodingitization of plagioclase cannot take place. Nozaka and Fryer (2011) suggested that coronitic replacement of olivine and plagioclase by tremolite and chlorite represents troctolite alteration at T > 450 °C. Temperatures in the root zone of the troctolite-hosted Kairei hydrothermal vent field are believed to be about 400 °C (Nakamura et al. 2009).

The temperature dependency of troctolite alteration has not been explored experimentally. In this contribution, we present the results of two new batch experiments specifically designed to investigate the alteration of olivine-rich troctolites at conditions where olivine serpentinizes (300 °C) and where it does not serpentinize (400 °C).

This is the peer-reviewed, final accepted version for American Mineralogist, published by the Mineralogical Society of America.
The published version is subject to change. Cite as Authors (Year) Title. American Mineralogist, in press.
DOI: https://doi.org/10.2138/am-2021-7832. http://www.minsocam.org/

92 # EXPERIMENTAL DESIGN & ANALYTICAL METHODS

93 ## Experimental techniques

94 We used a modified version of a Dickson-type hydrothermal apparatus (Dickson et al.
95 1963; Seyfried et al. 1987) to conduct two hydrothermal troctolite alteration experiments
96 at 300 and 400 °C (40 MPa). A mineral powder mix of forsteritic olivine (Fo91) and
97 anorthite-rich plagioclase (An95) in mass ratio of 3.5:1, was reacted with a deoxygenated
98 3.2 wt.-% NaCl solution inside a flexible gold reaction cell. Fluid samples were taken
99 repeatedly (initially prior to heating and after 10, 27, 49 and 76 days; final sample post
100 premature cooling) from the reaction cell and analyzed for salinity, pH, and concentrations
101 of dissolved ions as well as H_2 and CH_4. Solids were retrieved at the end of the experiment
102 after approximately 76 days. Details on the experimental design are included in
103 supplemental material M1.

104 ## Analytical techniques

105 Solute concentrations were measured by ICP OES (Agilent 720 – Si, Ca, Na) and
106 ICP MS (Thermo Finnigan Element2^{TM} – Mg, Al). Fluid aliquots for H_2 and CH_4
107 quantification were sampled into pre-weighed Hamilton® gastight glass syringes and
108 analyzed within 1 hour using an Agilent® 7820A Gas Chromatograph.
109 Solids were retrieved as a cemented concretion from the reaction vessel. Untreated
110 fragments were initially characterized via scanning electron microscopy (Zeiss SUPRA 40
111 FE-SEM equipped with a Bruker Modell XFlash 6 | 30 EDX) and the distribution of
112 porosity and of mineralogical variability were assessed by µ-CT scanning. . Cut slices of
113 the encrusted solid reactants were prepared as polished, carbon coated epoxy mounts for
114 additional SEM and EMPA work (Fig. 1). Detailed multi-element maps (Mg, Al, Fe, Ca)

115 of the mounts were prepared at Cardiff University on a Zeiss Sigma HD FEG-SEM
116 equipped with dual Oxford Instruments X-max 150 mm^2 energy dispersive silicon drift
117 detectors. EMPA analyses of mineral compositions were conducted with a CAMECA
118 SX100. All of the remaining material was crushed, homogenized and subjected to further
119 analysis including X-ray powder diffraction (XRD, Bruker D8 Advance). Bulk analysis of
120 solids prior to and after reaction were conducted via ICP-OES following acid digestion.
121 The fractions of alteration phases were estimated from phase characteristic dehydration
122 during thermogravimetric analysis (TG) using a NETZSCH STA 449 F3 Jupiter® Thermal
123 analyzer. The magnetite fraction was determined by magnetometric (AGFM)
124 measurements with a Princeton MicroMag™ 2900 Alternating Gradient Magnetometer
125 following the method described by Flanders (1988). Detailed specifications for all
126 analytical techniques are provided in supplemental material M1.

127 **Thermodynamic and kinetic modelling techniques**

128 Phase relations in the system MgO-CaO-SiO_2-Al_2O_3-H_2O were calculated with
129 Geochemist's Workbench® (GWB) (Bethke 2005), using a customized database (300,
130 400 °C – 50 MPa; attached as supplemental material M3.1). Activity-Activity diagrams
131 showing the phase relations in the system CaO-MgO-SiO_2-H_2O as well as CaO-Al_2O_3-
132 MgO-SiO_2-H_2O were prepared using ACT2 of the GWB® software package to evaluate the
133 fluid data from the experiments and from reaction path model predictions. Additional phase
134 relations for metastable anorthite-chlorite and forsterite-xonotlite reactions were derived
135 from log K values calculated with SUPCRT92 (Johnson et al. 1992), complemented with
136 thermodynamic data for xonotlite reported by Blanc et al. (2010).

Measured elemental concentrations and pH of fluid samples were used as input parameters for an EQ3NR speciation and subsequent heat-up to experimental conditions using EQ6 to obtain in-situ activities and pH. In-situ fluid pH and activities of Ca^{2+}, Mg^{2+} and SiO_2(aq) were computed using EQ3/6 (Version 8.0) (Wolery, 1992) with a customized database.

For reaction path modelling, the EQ3/6 database from Klein et al. (2013) was complemented with log K values for xonotlite. The log K values were calculated using SUPCRT92 (Johnson et al.,1992) and thermodynamic data from Blanc et al. (2010) (provided as supplemental material M3.2). Following an initial speciation and heating of the 3.2 wt.-% NaCl solution, reaction path modeling was conducted using the titration mode. In these simulations, a total amount of olivine-plagioclase mixture equal to the average W/R and composition used in the experiments was added to the fluid phase in small aliquots. Reaction progress is expressed through the dimensionless parameter ξ, which varies between 0 and 1. Details regarding thermodynamic modelling are included in supplemental material M1.

RESULTS

Time series evolution of fluid compositions

Characterization of concomitant fluid samples provided ad hoc information on the on-going reaction within the flexible gold reaction cells (see Fig. 2 and Table 1The last in-situ fluid samples were obtained after approximately 1200 hrs. The experiment continued for another 450 hrs, before a power failure occurred and the system cooled down. The solids were retrieved after another 48 hrs. . Hence, the in-situ fluid chemistry to go with the final solids is not known. But as the fluid composition appeared to reach a steady state

after 1200 hrs, it may not have been too dissimilar after 1750 hrs and can be reasonably assumed as representative of the fluid supernatant to the plug of cemented solids finally retrieved.

Incipient hydrolysis of olivine resulted in a sharp increase of Mg concentration (156 µmol/kg (µM)). Less pronounced were simultaneous increases of Si (32 µM), Ca (25 µM) and Al (7 µM), of which the latter two are due to incipient plagioclase dissolution. Major changes were observed after heating the experiments to 300 and 400 °C.

At 300 °C, Mg (to 15 µM) was rapidly depleted, while Si contents remained virtually unchanged (30 µM) and Ca concentrations increased to > 2 mmol/kg (mM) (see Fig. 2 A). All elements were subsequently depleted from the fluid. After 1200 hrs, Mg and Si levels were <10 µM, while Ca contents stayed well above 1 mM. Reactions at 300 °C involved a net consumption of H^+ ions that caused an increase in the fluid pH. Calculated in-situ pH increased from an initial 6.4 to a final value of 7.2 (pK_W at these *P T* conditions is 11.086). Increasing amounts of H_2 indicated significant oxidation of Fe^{2+} to Fe^{3+}, as is expected for serpentinization reactions. H_2 concentrations steadily increased to 20.5 mM after 1174 hrs. Small amounts of methane (< 40 µM) were also detected, which could have been produced through breakdown of organic contaminants or CO_2-reduction with H_2 (McCollom and Seewald, 2001).

In the 400 °C experiment Mg concentrations rapidly decreased, while Si concentrations continuously increased to about 0.8 mM after 1200 hrs (see Fig. 2 B). Calcium was initially enriched to more than 3.5 mM but decreased to a final level close to that observed in the 300 °C experimental run. Proton activity at 400 °C remained almost unchanged at near-neutral pH level around 6 (in-situ pK_W is 11.356) throughout the experiment. Initially, H_2

concentration increased to 4 mM (after 238 hrs), before returning to only 200 μM after 1200 hrs. Methane contents at 400 °C are 5-fold increased (max. 250 μM) relative to the 300 °C run. The increase in methane contents cannot explain the drop in H_2 levels, as 250 μM of methane from DIC would require no more than 1 mM of H_2. Moreover, methane concentrations also drop in the later stages of the experiment A summary of all fluid data is given in Table 1.

Fluid-mineral reactions

The solids retrieved from the two experiments were not muds as is commonly the case in serpentinization studies. Instead, the retrieved material was a hard, compact concretion that had formed at the bottom of the reaction cells. Oriented fragments of the concretion were selected for detailed documentation. The concretions are zoned in terms of mineralogical composition and the boundaries between different zones (α to ε in Fig. 1) are parallel to the solid-fluid interface in the autoclave (see Fig. 3 F). The mineralogical variability and zonations were characterized on cut polished sections and on untreated crust surfaces (see Fig. 1).

Fluid-mineral reaction in the 300 °C experiment. Bulk sample powder-XRD characterization revealed the presence of serpentine, brucite, magnetite, chlorite, xonotlite and andradite, in addition to unreacted forsterite and anorthite. SEM and EMP work showed that these phases form different assemblages in five domains (Fig. 3 A+B and supplemental Fig. S1).

The domain closest to the fluid-rock interface (α) was dominated by a typical serpentinization product mineral assemblage (serpentine, brucite, and magnetite) with additional chlorite (see Fig. 3 A, B and D). Former grain boundaries of primary olivine are

206 traced by a thin band of fine-grained chlorite (< 1 μm), which is the sole Al-bearing phase
207 in domain α. In some cases, remnants of olivine with distinct dissolution features are
208 preserved in the center of the cavities bordered by these chlorite rims (see Fig. 3 D+E). The
209 interstitial spaces between the proposed former grain boundaries were entirely cemented
210 with fine-grained serpentine and patches of xenomorphic brucite (see Fig. 3 D). In contrast,
211 the cavities left by apparently dissolved olivine or plagioclase are only partially filled with
212 serpentine and the cavity walls are covered with abundant microcrystalline magnetite (< 2
213 μm) forming euhedral octahedrally shaped crystals. In contrast, some additional
214 xenomorph iron (likely iron oxide or hydroxide) infrequently occurs in the completely
215 cemented interstitial space (see Fig. 3 E and Fig. S1). Brucite disappears at the transition
216 from domain α to domain β (see Fig. 3 A+B). Significantly larger portions of unreacted
217 olivine are present in domain β and the chlorite rims around them are thicker. Like in α,
218 serpentine is the dominant phyllosilicate. Microtomographic images of the intact
219 concretion show low porosities for domains α (2 vol.-%) and β (4 vol.-%) (see
220 supplemental Fig. S5.1). Hence, most of the chlorite-lined cavities seen in thin-section
221 were filled with relict olivine crystals that have been plucked during the polishing of the
222 mount. Such plucking is a common phenomenon due to the stark contrast in hardness
223 between olivine and serpentine (±chlorite). We assume that this plucking was more limited
224 in β as chlorite rims were thicker.

225 SEM work on an untreated crust fragment representing the interface of the top
226 section of the concretion with the cell wall shows a mixture of serpentine and subordinate
227 chlorite that covers almost the entire surface. But in contrast to the inner parts of domains
228 α and β, hydroandradite (X_{Fe} = Fe / (Fe + Al) = 0.98), and not magnetite, is the dominant

Fe-phase. Idiomorphic, rhombic dodecahedron-shaped crystals (2-4 μm) of hydroandradite may cluster in dense aggregates (Fig. 3 C). This occurrence of andradite is entirely restricted to a thin layer representing the interface to the cell wall.

The transition between domains β and γ is marked by significant drop in magnetite abundance (see Fig. 3 A+B). Instead, domain γ contains major portions of unreacted olivine. Serpentine is less abundant and chlorite is the dominant phyllosilicate forming thick coronas around primary olivine. Interstitial void space makes up significant portions of this domain and we suspect that these voids were in part created by anorthite dissolution. Microtomography confirms a considerable porosity for domain ε (16 vol.-%), so significant plucking can be ruled out. In domain δ these voids are partly to completely filled by xonotlite (Fig. 3 A+B). Magnetite is rare and the fraction of unreacted olivine (max. 30 μm) is clearly subordinate to the alteration phases. The chlorite rims around the olivine relics are again notably thicker (up to 20 μm) than in domain γ (Fig. 3A). Where chlorite in the interstitial space occurs as less dense aggregates, it exhibits a characteristic edge-to-face arrangement of small individual flake-shaped crystals (see Fig. 4 H). In contrast to domain α – γ, the interstitial space in domain δ is almost completely cemented by acicular xonotlite crystals, up to 80 μm long (see Fig. 3 G+H). Domain ε shows abundant primary anorthite, which is completely absent in all other domains (Fig. 3 A+B). A close to original size and shape of anorthite crystals (up to 100 μm, recognizable crystal planes) indicates a very limited plagioclase dissolution in this domain. At the same time olivine is rare and leftover relics exhibit the thickest chlorite coatings of all domains. Interstitial space is partly cemented with xonotlite like in domain δ, but the overall xonotlite abundance is decreased in domain ε.

We summarize the most striking differences in the five domains (α – ε): (1) There is no Ca-bearing alteration phase in domains α – γ and anorthite is restricted to domain ε. (2) The abundance of chlorite as the sole Al-bearing mineral is low in domains α – β and much increased in the inner domains (δ and ε); the thickness of chlorite rims increased markedly from outside to the inside. These variations come with chemical differences between the inner domains that are Ca- and Al-rich and the outer domains of the concretion, which are Mg- and to a lesser extend Fe-rich.

The compositions of the relict olivine ($Mg_{1.82}Fe_{0.18}SiO_4$; X_{Mg} = Mg / (Mg + Fe) = 0.91) and anorthite (X_{Ca} = Ca / (Ca + Na) = 0.96) from the 300 °C experiment are unchanged relative to the compositions of the reactants. Brucite ($Mg_{0.93}Fe_{0.07}(OH)_2$; X_{Mg} = 0.93) and especially serpentine ($Mg_{2.92}Fe_{0.08}Si_2O_5(OH)_4$; X_{Mg} = 0.973) found in domain α are enriched in Mg compared to olivine, which is in line with the abundant presence of magnetite. Chlorite compositions ($Mg_{4.54}Fe_{0.44}Al_{1.51}Si_{3.35}O_{10}(OH)_8$; X_{Mg} = 0.91) show no systematic differences between domains. Most analyses reveal a reduced fraction of Al and slightly increased Si, which may indicate minor but common intergrowth with serpentine or saponite (see Fig. 4). Chlorite has an X_{Mg} of 0.91, similar to the olivine it replaced. This explains the lack of magnetite, which is not needed as Fe-host in the chlorite-rich inner domains (δ and ε). Xonotlite compositions are uniform ($Ca_{6.03}Fe_{0.06}Al_{0.39}Si_{5.65}O_{17}(OH)_2$) and indicate minor substitution of Si by Al. Average mineral compositions are provided in Table 2.

Fluid-mineral reaction in the 400 °C experiment. X-ray powder diffraction indicated relict olivine and plagioclase and secondary chlorite, serpentine, xonotlite as well as andradite, grossular and diopside. While all phases were observed in different domains

in the SEM/EMP surveys, unlike in the 300 °C experiment, these domains in the cemented solids do not simply follow a top-to-bottom layered sequence. The successive collapse of the gold cell following repeated fluid sampling has led to a certain degree of folding and compaction of the solid material but a differentiation of the different domains in terms of isolation and association between each other is still possible (Figs. 1 and S2). Domain α* contains large portions of unreacted olivine in addition to a mixture of chlorite ±serpentine as well as clinopyroxene (see Fig. 5 A+B). Domain α* is in itself very heterogeneous as the proportions of minerals change significantly towards the boundary to the adjacent domain β* (see supplemental Fig. S2). Towards this boundary olivine relics exhibit an increasingly thick chlorite coating. Next to the chlorite, large euhedral clinopyroxene crystals (up to 100 µm in length) grew as a cementitious phase in the intergranular void space. Euhedral isometric crystals (up to10 µm in diameter) of andradite-rich hydrogarnet (X_{Fe} = 0.81) are commonly associated with clinopyroxene (see Fig. 5 C). The abundance of all three secondary phases increases towards the adjacent domain β* while unreacted olivine becomes less abundant. As in the 300 °C experiment, a particularly large discrepancy between the apparent (polished mount surface, Fig. 5 A) and actual porosity (µ-CT; Fig. S5.2) for domains α and β, as well as a similarity in cavity and olivine crystal shapes, indicates that the true share of unreacted olivine is much higher (see supplemental Tab. S1). Domain β* is comprised of pseudomorphic chlorite after olivine and cementing clinopyroxene as well as andradite (see Fig. 5 A+B). The boundary between domains β* and γ* is not gradual as clinopyroxene suddenly disappears and prismatic xonotlite crystals (up 90 µm in length) are instead developed as void fill (see Fig. 5 A+B). At the same time the hydrogarnet composition changes to hydrogrossular-rich (X_{Fe} = 0.23). Moreover, the

298 cementation appears much more compact than in domains α* and β* as xonotlite fills most
299 voids and fine-grained chlorite almost completely fills the center of former olivine grains.
300 Unreacted anorthite persists in domain δ*, (see Fig. 5 A+B) and the interstitial space is
301 cemented by xonotlite (see Fig. 5 E).

302 Two distinguishable parts in the studied untreated fragment representing the contact
303 to the cell wall resemble domains identified in the cut section (see Fig. 1 and Fig. 5 D).
304 The upper part appears most similar to domain β* ± α*, as it is comprised of clinopyroxene,
305 andradite and chlorite ± serpentine. But in contrast to domain β* ± α*, unreacted olivine is
306 absent and this outer contact surface is almost exclusively comprised of massive
307 clinopyroxene with minor andradite-rich hydrogarnet and accessory chlorite ± serpentine
308 in between clinopyroxene crystals (see upper right of Fig. 5 D). The lower part resembles
309 domain γ*, as it is exclusively comprised of chlorite, grossular and xonotlite. But again,
310 there is a shift in the relative proportions of the minerals with abundant chlorite, common
311 grossular-rich hydrogarnet and rare xonotlite (see Fig. 5 D).

312 In summary, the outside-to-inside variation in mineral abundance is as follows: (1) olivine
313 is partly preserved on the outside, where chlorite and Ca-silicates are rare. (2)
314 Clinopyroxene is very abundant in a zone that starts just underneath the top of the mineral
315 pile. (3) Anorthite is partly preserved in the innermost zone; xonotlite bridges between
316 clinopyroxene and anorthite. (4) Hydrogarnet is present throughout and is andraditic in the
317 outside and grossularian in the inside parts of the concretion; it is the most abundant Fe-
318 phase.

319 The compositions of unreacted olivine and anorthite also remained unchanged in
320 the 400 °C experiment and the compositions of alteration phases did not deviate between

domains (see Table 3). Several chlorite analyses exhibit a reduced Al fraction, indicating minor intergrowth with serpentine. Chlorite is somewhat more magnesian than the olivine reactant ($Mg_{4.59}Fe_{0.42}Al_{1.49}Si_{3.36}O_{10}(OH)_8$; X_{Mg} = 0.92; see Fig. 4). In contrast, the clinopyroxene composition ($Ca_{1.00}Mg_{0.86}Fe_{0.14}Si_2O_6$) reveals a significant hedenbergite component. Garnets could be subdivided into two groups. Those associated with clinopyroxene were always dominated by andradite ($Ca_{2.99}Al_{0.37}Fe_{1.54}Si_{3.01}O_{12}$; X_{Fe} = Fe / (Fe + Al) = 0.81). The zones in β* and α* that are rich in clinopyroxene and andradite are hence also somewhat enriched in Fe. The Al-rich garnet ($Ca_{2.98}Al_{1.58}Fe_{0.47}Si_{2.88}O_{12}$; X_{Fe} = Fe / (Fe + Al) = 0.23) is exclusively associated with xonotlite. Totals of the garnets scatter around 97 % indicating a small but noticeable katoite component ($SiO_4^{4-} \leftrightarrow 4(OH)^-$) in these hydrogarnets.

Mass balancing of the overall reactions

Mineral proportions in the bulk solid retrieved from the two experimental runs were estimated via mass balancing. First, the absolute mass fractions of water-bearing phases and magnetite contributions were quantified via TG and AGFM. The abundances of the remaining identified phases were subsequently estimated from stoichiometric considerations utilizing the measured compositions In the solid assemblage retrieved from the 300 °C experiment, characteristic dehydration events in the thermogravimetric analysis corresponded to 3.39 wt.-% of brucite and another 64.7 wt.-% of chlorite + serpentine (Földvári 2011; Trittschack et al. 2014). The magnetite fraction derived from multiple AGFM analyses corresponded to 2.40 ± 0.3 wt.% of the total mass. The proportions of the remaining phases were reconstructed from stochiometric considerations and balancing of elemental budgets. The details of this procedure are provided in supplemental material M4.

The results are given in Table 4 and match the observations made during the investigation of the cut sections. Reaction turnover based on this mass balance would be 77.5% by weight.

For the 400 °C experiment, thermogravimetric analysis yielded only one characteristic dehydration that corresponds to 38.21 wt.-% of chlorite and serpentine. Although magnetite was not observed during EMP and SEM surveys, AGFM analysis clearly indicated the presence of a ferrimagnetic component, yet the corresponding magnetite fraction would not contribute more than 0.03 wt.%. The share of the remaining phases was deduced following a balancing of elemental budgets similar to that used for the 300 °C experiment with details given in supplemental material M4. The results provided in Table 4 indeed appear quite reasonable as some parts of domain α* in the investigated section were almost exclusively comprised of unreacted olivine whereas overall lesser amounts of relict plagioclase were observed (see Fig. 5 and supplemental Fig. S2). Reaction turnover based on this mass balance is 52.2% by weight.

Implications from reaction path modeling

Reaction path modeling for both experimental runs was conducted using the EQ3/6 computer code to compare the experimental findings with equilibrium model predictions. Details of the exact parameterization of the model runs and all underlying assumptions are provided in supplemental material M4.

At 300 °C, the reaction path model predicted a typical serpentinization product mineral assemblage, including serpentine-ss (solid solution of chrysotile, greenalite and cronstedtite), brucite-ss, and magnetite, in addition to clinopyroxene-ss (solid solution of diopside and hedenbergite) and chlorite-ss (solid solution of clinochlore and daphnite). The

one major difference to the assemblage produced in the 300 °C experiment is that the model initially predicts diopside instead of xonotlite and several Ca bearing phases had to be suppressed in the model before apparently metastable xonotlite was predicted (see Fig. 6 A and supplement M4). But considering that the observed zonation is a clear sign of a not fully equilibrated system, the proportions of different mineral phases that are indicated for the calculated reaction turnover of 77.5% by weight resemble the proportions derived from analyses and mass balancing (see Table 4).

At 400 °C, the predicted mineral assemblage, mainly consisting of chlorite-ss, clinopyroxene-ss, serpentine-ss, as well as a large fraction of unreacted olivine is in good agreement with the documented solid reaction products (see Table 4). A mismatch between model and observation concerns magnetite, which was predicted to form instead of the ubiquitously disseminated andradite-dominated garnet observed in the studied section. The model run also produced a very iron-rich serpentine (large cronstedtite component), and the serpentine-chlorite mixture from the experiment was depleted in Fe. Then again, a complete absence of cronstedtite cannot be concluded as a very Mg-rich chlorite dominates in the serpentine-chlorite mixture and this could mask the presence of the Fe-serpentine. If these Fe phases are suppressed, however, garnet is predicted and for a reaction turnover of 55.2% by weight (ξ of 0.69), predicted resemble the observed mineral proportions (see Fig. 6 B and Table 4), albeit the fraction of unreacted plagioclase is strongly overpredicted (32% versus 9% indicated by mass balance).

Differences between measured and modeled assemblages for both temperature levels highlight, how a simple equilibrium thermodynamic titration path can obviously not

fully explain the dissimilar mineral assemblages in the multiple domains that developed in the experiments.

DISCUSSION

Interpretation of mineralogical observations, phase relations and fluid data

The temporal evolution of fluid composition reflects both the type and extent of mineral-fluid reactions within the gold cell. Investigating corresponding phase relations is most conveniently accomplished by plotting the *in-situ* activities of reactant solutes in phase diagrams that also depict the stability fields of mineral assemblages in the fluid-rock system under the relevant *p-T* conditions. Compositional trajectories of fluids predicted by the comparative reaction path models can be complemented.

Phase relations at 300 °C. The initial fluid has low silica, coincidentally close to the serpentine-brucite univariant line, and very low Ca^{2+} contents (see Fig. 7; Table 1: T.1.1). Upon reaction with olivine and plagioclase, the measured composition evolves towards higher Ca^{2+} activities, while silica activity remains close to the serpentine-brucite univariant line. Olivine reacts to serpentine and brucite (rxn.1) and simultaneously the dissolution of plagioclase provides sufficient Al for the formation of chlorite, from either olivine (rxn.2) or serpentine (rxn.3).

$$2\,Mg_2SiO_4 + 3\,H_2O \rightarrow Mg_3Si_2O_5(OH)_4 + Mg(OH)_2 \qquad \text{rxn. 1}$$

$$2\,CaAl_2Si_2O_8 + 5\,Mg_2SiO_4 + 6\,H_2O + 4\,H^+ \rightarrow 2\,Mg_5Al_2Si_3O_{10}(OH)_8 + 3\,SiO_2(aq) + 2\,Ca^{2+} \qquad \text{rxn. 2}$$

This is the peer-reviewed, final accepted version for American Mineralogist, published by the Mineralogical Society of America.
The published version is subject to change. Cite as Authors (Year) Title. American Mineralogist, in press.
DOI: https://doi.org/10.2138/am-2021-7832. http://www.minsocam.org/

$$3\,CaAl_2Si_2O_8 + 5\,Mg_3Si_2O_5(OH)_4 + 6\,H^+ \rightarrow 3\,Mg_5Al_2Si_3O_{10}(OH)_8 + 7\,SiO_2(aq) + 3\,Ca^{2+} + H_2O \quad \text{rxn. 3}$$

Reactions of plagioclase release Ca and consume protons, which elevates log (aCa^{2+}/a^2H^+). Silica is also released, but its activity is fixed by the reaction of brucite to serpentine (rxn. 4).

$$3\,Mg(OH)_2 + 2\,SiO_2(aq) \rightarrow Mg_3Si_2O_5(OH)_4 + H_2O \quad \text{rxn. 4}$$

Such silica buffering can only be explained if olivine reacts in excess of plagioclase and mass balancing confirms that 7.4 moles olivine serpentinized while 1 mole of plagioclase reacted.

In contrast, the model had olivine and plagioclase react in exactly the initial proportions (ol/plg = 6.7) and the interacting model fluid initially showed an early spike to higher log $aSiO_2(aq)$ (see Fig. 7). But after less than 1 wt.% reaction turnover ($\xi << 0.01$), the model fluid composition meets the univariant serpentine-diopside line or, if diopside and garnet are suppressed, the xonotlite-in line (rxn. 5; see Fig. 7).

$$6\,SiO_2(aq) + 6\,Ca^{2+} + 7\,H_2O \rightarrow Ca_6Si_6O_{17}(OH)_2 + 12\,H^+ \quad \text{rxn. 5}$$

Further reaction will have compositions follow the univariant line towards an even higher log (aCa^{2+}/a^2H^+) and a lower log $aSiO_2(aq)$ until they reach the intersection with the brucite – chrysotile phase boundary (see Fig. 7). After <20 wt.-% reaction turnover the fluid composition is buffered by serpentine, chlorite, magnetite, xonotlite and brucite. The formation of xonotlite alongside chlorite can also be written as a desilication of plagioclase. As outlined before (rxn. 2 and 3), both serpentine or olivine can source Mg but the two

This is the peer-reviewed, final accepted version for American Mineralogist, published by the Mineralogical Society of America.
The published version is subject to change. Cite as Authors (Year) Title. American Mineralogist, in press.
DOI: https://doi.org/10.2138/am-2021-7832. http://www.minsocam.org/

423 reactions (rxn. 6 and rxn. 7) are essentially linked through the serpentinization reaction
424 (rxn. 1).

$$6\,CaAl_2Si_2O_8 + 15\,Mg_2SiO_4 + 25\,H_2O \rightarrow\ Ca_6Si_6O_{17}(OH)_2 + \ 6\,Mg_5Al_2Si_3O_{10}(OH)_8 + \ 3\,SiO_2(aq) \qquad \text{rxn. 6}$$

$$6\,CaAl_2Si_2O_8 + 10\,Mg_3Si_2O_5(OH)_4 + 5\,H_2O \rightarrow\ Ca_6Si_6O_{17}(OH)_2 + \ 6\,Mg_5Al_2Si_3O_{10}(OH)_8 + \ 8\,SiO_2(aq) \qquad \text{rxn. 7}$$

425 As long as log $aSiO_2(aq)$ remains below -1.59, reactions 6 and 7 will be exergonic
426 (see Fig. 7). Excess olivine in the s will sustain continuous brucite production, which
427 buffers silica activity at sufficiently low levels (rxn. 4). Indeed, high amounts of brucite,
428 serpentine and magnetite were observed in the experiment. This is due to the high olivine
429 proportion in the starting material. The molar ratio of plagioclase to olivine required for
430 reactions 2, 3, 6 and 7 are ≤ 1:2.5 compared to an actual reaction ratio of 1:7.4 indicated
431 by mass balance. The olivine reactant also had a considerable fayalite component (X_{Mg} =
432 0.91), whereas serpentine and brucite from domain α were both depleted in Fe (X_{Mg} = 0.96
433 respectively 0.93). This observation is in line with the ubiquitous presence of additional
434 magnetite in domain α and high $H_2(aq)$ concentrations measured in the fluid samples. A
435 serpentinization reaction for the 300°C experiment can be given as:

$$2\,Mg_{1.813}Fe_{0.187}SiO_4 + 2.84\,H_2O \rightarrow Mg_{2.917}Fe_{0.083}Si_2O_5(OH)_4 + 0.76\,Mg_{0.932}Fe_{0.068}(OH)_2 + 0.08\,Fe_3O_4 + 0.08\,H_2(aq) \qquad \text{rxn. 8}$$

This is the peer-reviewed, final accepted version for American Mineralogist, published by the Mineralogical Society of America.
The published version is subject to change. Cite as Authors (Year) Title. American Mineralogist, in press.
DOI: https://doi.org/10.2138/am-2021-7832. http://www.minsocam.org/

436 The observed distribution of iron is also in agreement with bulk fluid composition
437 and CaO-FeO-SiO_2-H_2O-H_2 phase relations at 300°C. The speciated fluid samples are
438 likely most representative of the intergranular fluid in α and β and plot well within the
439 magnetite stability field (see Fig. 7; T1.2 – T1.4). In contrast to the outermost domain α,
440 serpentine also does not occur as a pure Mg-poor chrysotile-greenalite component but only
441 in combination with chlorite in the inner domains (γ to ε). The mixture of both phases has
442 an overall X_{Mg} that is identical to that of the olivine reactant and hence ferrous iron (Fe^{2+})
443 was not available for oxidation and the formation of magnetite.

444 **Development of a mineral zonation at 300 °C.** Computational results confirm that
445 the observed mineral phases can be expected at the experimental conditions. However, a
446 bulk equilibrium model cannot reproduce the complex mineral zonation documented in the
447 retrieved solids. Why are magnetite and brucite restricted to the outer domains (α and β),
448 whereas xonotlite is only present in the inner domains (δ and ε)? We hypothesize that the
449 zonation developed as different portions of the solids reacted at variable rates due to
450 differences in the degree to which the bulk fluid could mix and homogenize with local
451 intergranular fluid. As there is no temperature gradient throughout the reaction cell, there
452 will be no fluid flow or convective mixing but only diffusive exchange between adjacent
453 fluid volumes. As the water-rock reaction proceeds throughout the solid volume, the local
454 intergranular fluid evolves towards saturation with respect to the local mineral assemblage.
455 With the solid reactants at the bottom of the cell, the intergranular fluid in the uppermost
456 portions of the reactants is in direct contact with the overlying bulk fluid (see Fig. 3 F).
457 The fluid in this portion is quickly diluted through diffusive mixing. In contrast, the dilution
458 of the intergranular fluid further towards the bottom of the cell can be expected to proceed

459 slower as there is an overlying batch of solid and fluid reactant separating it from the bulk
460 fluid. Therefore, the intergranular fluid further towards the bottom would quickly become
461 saturated with respect to the local assemblage slowing further reaction progress. In
462 contrast, the reaction can be expected to proceed faster in the uppermost portions of the
463 solid reactants. Regardless of this premise, plagioclase reacting next to serpentinizing
464 olivine throughout the assemblage initially represented a source of Al for the formation of
465 chlorite instead of serpentine (rxn. 2 and rxn. 3). Consequently, we observe thin chlorite
466 coronas around relict olivine grains in domains α and β (see Fig. 7 A). This replacement of
467 olivine by chlorite requires a certain fluid mobility of Al. And a similar initial chlorite
468 formation can be assumed at the bottom of the cell, only somewhat slower due to the
469 mechanism described above. This early cementation through the formation of chlorite
470 would arguably further limit the exchange between the bulk fluid and the intergranular
471 fluid in the lower portions of the solid reactants. As the much less abundant plagioclase
472 reactant inevitably is exhausted in the faster-reacting outer domains, chlorite can no longer
473 form and hence the chlorite coronas remain comparably thin. More importantly, this
474 exhaustion of plagioclase also constitutes a major change with respect to the local buffering
475 of the water-rock reaction. As the reaction proceeds, an increasing portion of the solids
476 closer to the bulk fluid – solid interface will be exclusively buffered by unreacted olivine
477 and this has manifold implications (see Fig. 3 F):

478 (1.) Further reaction of remaining olivine subsequently produces a pure
479 serpentinization mineral assemblage of serpentine, brucite and magnetite in these domains
480 (see Fig. 7 A; rxn. 8).

(2.) This serpentinization of olivine can be expected to proceed slower as there is no longer a local stark chemical contrast between the original reactants in which the serpentinization of olivine is fueled by the desilication of plagioclase. Taking into account that a major share of the cavities visible in domains α and β of the investigated mount were in fact filled with unreacted olivine (as indicated by μ-CT scans, see supplemental Fig. 5.1), we can conclude that olivine reaction in the outer domains α, β and γ ultimately was much less complete than in the innermost domains δ and ε (see Fig. 3 A+B).

(3.) At this stage considerable fractions of unreacted plagioclase were still present in the solids more towards the bottom of the reaction cell. As a consequence, a chemical potential gradient could have been established between the more isolated portions of the solids (buffered by olivine and plagioclase - chlorite) and the domains closer to the solid fluid interface (buffered by olivine – serpentine, brucite, magnetite ±chlorite) (see Fig. 3 F). To explore whether this proposed gradient resulted in a mass exchange between the inner and outer domains, an additional mass balance was prepared for the individual domains, based on SEM maps (see Fig. 3 A, supplementary Fig. S4.1-S4.3 and Table S1). This evaluation confirms that the different domains systematically differ with respect to individual elemental abundances and that a selective mass transfer must have occurred (see Fig. S4.2). While Si is distributed uniformly, Ca and Al are strongly depleted in the outer domains α and β, but very abundant in the inner domains δ and ε towards the bottom of the reaction cell. In contrast, Mg – and to a lesser extent Fe – are depleted in the interior but enriched in the outer domains α to β.

Plagioclase dissolution in the outer domains also released Ca, which was partially reflected in the initial spike in the fluids' Ca concentration; however, the lack of any Ca-

504 bearing phase in domains α to γ indicates that most of the Ca was eventually transferred to
505 the inner domains. Possibly, the Ca concentration simply remained below the level
506 necessary for xonotlite formation in the uppermost layer of the solids by the time of
507 plagioclase exhaustion (see Fig.3 A+B and Fig. 7, rxn. 5). Later, the local buffering by the
508 serpentine-brucite-magnetite assemblage and the absence of a precursor Ca mineral surface
509 could have actively prevented precipitation of a Ca-bearing mineral phase in the outer
510 domains. In the moderately isolated domain γ, a somewhat delayed incipient growth of
511 chlorite coronas is facilitated by Al supplied through limited diffusional equilibration with
512 the faster reacting domains α and β. As mass balancing indicates a faster reaction of olivine
513 compared to plagioclase, this externally sourced Al boosts the growth of chlorite. In
514 contrast to domains α and β, domain γ contains a considerable share of true porosity and
515 the shape of the pores more closely resembles the interstitial space which is filled with
516 xonotlite and plagioclase in the most isolated domains (see Fig. 3 A+F and supplemental
517 Fig. 5.1). Domain γ represents the connecting micro environment between the differently
518 buffered poles of the documented zonation, in which the plagioclase reactant ultimately
519 could completely dissolve but xonotlite formation might have been prevented through the
520 vicinity of the directly adjacent serpentine - brucite - magnetite buffered domain. At this
521 stage the comprehensive serpentine cementation in the outer domains and compaction
522 under high pressure resulted in further reduction of porosity to a degree where exchange
523 with the bulk fluid became very limited and a batch of intergranular fluid became locked-
524 in within the inner portions of the solids (see Fig. 3 B+F and supplemental Fig. S5.1). In
525 the inner domains δ and ε, a of time-integrated diffusive influx of Ca, further dissolution
526 of abundant plagioclase and a lack of fluid dilution eventually pushed the system to

supersaturation with respect to xonotlite. Xonotlite clearly precipitates in the intergranular space from a supersaturated solution and does not replace one of the primary phases (see Fig. 3 A+B and Fig. 7 B). Regarding the influx of Ca to domains δ and ε (see supplemental Table S1 and Fig. S4.2), one explanation for the directed mass transfer could be that once the high threshold for xonotlite crystal formation was breached in the innermost domains, further precipitation at existing crystal surfaces required much lower Ca levels and this would then constitute a sink for dissolved Ca. A pronounced inward directed flux of Ca^{2+} ions was apparently balanced by an outward directed flux of Mg^{2+} ions. In fact, mass balancing corroborates this hypothesis and the in-to-out flux of Mg^{2+} would facilitate the observed serpentine and brucite cementation in the outer domains (α + β) (see Fig. 3 A+D and suppl. Fig. S4.2). Similar to the explanation for Ca flux, the serpentine – brucite – magnetite buffered domains α and β provided conditions that allowed magnetite to crystallize and hence, these domains became a sink for Fe (see Fig. 3 D+E and supplemental Fig. S.4.2). On the opposite end, the diffusion-related surplus of Al and late reaction of plagioclase translates to ever thicker chlorite coronas around relict olivine in domains δ and ε. Serpentine did not precipitate in the intergranular space and is hence not part of the (meta) stable mineral assemblage in and around the pore space. In domain δ, where plagioclase is completely reacted, serpentine is limited to the space between thick chlorite coronas and relict olivine (see Fig. 3 H). In the innermost domain ε, olivine is closely armored by chlorite coronas indicating that as long as plagioclase provided an immediate source of Al, serpentine formation is effectively prohibited (see Fig. 3 I). Successive isolation through cementation increasingly decelerated the reaction progress so

This is the peer-reviewed, final accepted version for American Mineralogist, published by the Mineralogical Society of America.
The published version is subject to change. Cite as Authors (Year) Title. American Mineralogist, in press.
DOI: https://doi.org/10.2138/am-2021-7832. http://www.minsocam.org/

549 that upon termination of the experiment, larger portions of anorthite remained unreacted in
550 the innermost domain ε.

551 **Interpretation of phase relations, fluid data and zonation at 400 °C.** At 400
552 °C, forsterite is part of the equilibrium mineral assemblage instead of brucite and silica
553 activity is hence buffered at a higher level. Mass balancing indicates that ≥90% of
554 plagioclase reacted, while more than 60% of olivine remained unreacted. The in-situ
555 speciated fluids are in equilibrium with a forsterite-chlorite assemblage (see Fig. 8). But
556 the reaction path model fluid quickly hits the univariant forsterite - diopside phase
557 boundary as plagioclase dissolves (see yellow path in Fig. 8). Silica released by plagioclase
558 dissolution facilitates some direct reaction of olivine to serpentine (rxn. 9), which is
559 intergrown with chlorite.

$$3\,Mg_2SiO_4 + SiO_2(aq) + 4\,H_2O \rightarrow 2\,Mg_3Si_2O_5(OH)_4 \qquad \text{rxn. 9}$$

560 However, the extent of olivine alteration in the outermost domain α* is very small
561 and limited to the formation of chlorite coronas (rxn. 2 and 3). This is in contrast to the
562 extensive replacement of olivine by serpentine-brucite in the 300 °C experiment and
563 suggests that the olivine reaction progress at 400 °C is strictly controlled by plagioclase
564 dissolution.

565 While the sampled fluid never reached diopside saturation, the model fluid does
566 reach the univariant forsterite - diopside line and precipitation of diopside in addition to
567 chlorite is predicted (see Fig. 8). A simplified overall hydration reaction can be defined:

$$CaAl_2Si_2O_8 + 3\,Mg_2SiO_4 + 4\,H_2O \rightarrow Mg_5Al_2Si_3O_{10}(OH)_8 + CaMgSi_2O_6 \qquad \text{rxn. 10}$$

568 Texturally, chlorite replaces olivine and clinopyroxene precipitates in the void
569 space created by plagioclase dissolution. The main observed Fe-phase in the outer domains
570 was andradite. The position of the model fluids in Fig. 8 indicates that magnetite should be
571 the stable Fe-phase. However, the univariant lines were constructed for unity activities of
572 all reaction components. The andradite-magnetite boundary will shift downwards if lower
573 H_2(aq) activities are assumed (Fig. 8; rxn. 11).

$$2\ Fe_3O_4 + 9\ Ca^{++} + 9\ SiO_2(\text{aq}) + 10\ H_2O \rightarrow 3\ Ca_3Fe_2Si_3O_{12} + 18\ H^+ + H_2(aq) \qquad \text{rxn. 11}$$

574 Indeed, low H_2 contents were detected in the 400 °C fluids (Tab. 1), so the presence
575 of andradite is not unexpected. Andradite can be an indicator for low temperature
576 serpentinization environments (<220 °C), but it is stable at higher temperatures if brucite
577 is not stable (Frost and Beard, 2008). Our results support the notion of possible andradite
578 formation at T > 340 °C, the upper stability limit of brucite (McCollom and Bach, 2009).
579 The chlorite-clinopyroxene product mineral assemblage and the relative stability of
580 the olivine reactant (bar some reaction to serpentine) in the outer domains α* and β*
581 constitutes a major share of the reaction turnover in the 400 °C experiment. As in the
582 300 °C run, the reaction can be expected to proceed somewhat faster in the uppermost
583 portion of solids (see Fig. 3 F). Likewise, it can be expected that the local buffering of the
584 system within the uppermost layers shifted upon plagioclase exhaustion. But in contrast to
585 the 300 °C experiment, olivine was stable after plagioclase had reacted away. The resulting
586 conditions allowed for the Ca-phase diopside to crystalize (see Fig. 5 A+B). As supported
587 evaluation of porosity, olivine stability also prevented a subsequent comprehensive
588 cementation of domains α and β and the inner domains arguably did not become as isolated

This is the peer-reviewed, final accepted version for American Mineralogist, published by the Mineralogical Society of America.
The published version is subject to change. Cite as Authors (Year) Title. American Mineralogist, in press.
DOI: https://doi.org/10.2138/am-2021-7832. http://www.minsocam.org/

as in the 300 °C experiment (compare supplementary Fig. S5.1 and S5.2). Nonetheless the bipolar system of differently buffered water-rock reactions in the upper- and lowermost portions of the solids was also established at 400 °C. Mass balancing the elemental abundances in the individual domains confirms that Ca and Al were transferred inwards, while Mg abundance was overall increased in the outer domains (see supplemental Fig. 4.4 and Table S1). The Mg-free phases grossular, and xonotlite were observed in the inner domains γ* and δ*. As in the 300 °C experiment, we assume that Ca activities were elevated towards the inner domains due to limited dilution with the bulk fluid and active mass transfer from the outer domains. Reaction of plagioclase with the Ca enriched fluids in the inner domains resulted in the observed precipitation of xonotlite and grossular in the intergranular space (see Fig. 8 B; rxn. 12).

$$CaAl_2Si_2O_8 + 8\,Ca^{++} + 7\,SiO_2(\text{aq}) + 9\,H_2O \rightarrow Ca_3Al_2Si_3O_{12} + Ca_6Si_6O_{17}(OH)_2 + 16\,H^+ \quad \text{rxn. 12}$$

Finally, a feature observed at both temperatures is the inward increase in the width of chlorite coronas around olivine.

Experimental results compared to natural troctolite alteration

Overall, the experimental results are in good agreement with the conclusion by Frost et al. (2008) that troctolite alteration is predominantly dictated by the contrasting interplay between the serpentinization of olivine and the alteration of plagioclase. Specifically, strong contrasts in buffering of the water-rock reaction in variably fast reacting portions of the solids appear to be key for generating driving force for the reaction and mass transfer. Close to the solid-fluid interface where the less abundant plagioclase is

609 eventually completely reacted, exclusive serpentinization of olivine to serpentine and
610 brucite imposes locally extremely low silica activities and the intergranular fluid is
611 buffered by the assemblage serpentine - brucite - magnetite. In natural olivine-rich rocks,
612 this reaction dominates the composition of intergranular fluids and the alteration of
613 plagioclase is desilication to prehnite and hydrogrossular. This is similar to what drives
614 rodingitization reactions (e.g., Bach and Klein, 2008). Frost et al. (2008) and Nozaka and
615 Fryer (2011) found two types of troctolite alteration: (1) the microrodingite type in which
616 olivine is replaced by serpentine and plagioclase is altered to prehnite / hydrogrossular, and
617 (2) a higher-grade type, in which coronas of chlorite (replacing plagioclase) and tremolite
618 (after olivine) develop at the former plagioclase-olivine grain boundaries. Considering the
619 estimated lower alteration temperature for the microrodingitized troctolites from the
620 Atlantis Massif (<350 °C), they likely provide a better analogue for the 300 °C experiment.
621 The 400 °C experiment did not produce tremolite. In both experiments the alteration
622 produced significant amounts of serpentine, chlorite and magnetite, however, xonotlite and
623 clinopyroxene (at 400 °C) were the most abundant Ca-silicates formed in the experiments,
624 while in the Atlantis Massif samples serpentinization yielded prehnite and grossular. It
625 should be noted that an early chlorite-tremolite assemblage after olivine and plagioclase
626 was documented for both Atlantis Massive troctolite alteration types, including the
627 microrodingites. As the prehnite and grossular assemblage overprinted this earlier
628 assemblage, its existence may well have been a necessary condition for the formation of
629 the observed alumosilicates. But Nozaka and Fryer (2011) also deduced formation
630 temperatures between 400 and 650 °C for the early chlorite-tremolite assemblage and this
631 would exclude a similar alteration sequence for our experiments. Another explanation for

this discrepancy might be that a powder sample was used in the experiment, whereas a compact rock reacted in the natural system. Prehnite (Ca/Si = 0.67) and grossular (Ca/Si = 1) are proposed to result from a 1st and 2nd step of consecutive desilication of plagioclase (Ca/Si = 0.5), which is driven by low silica activities imposed by serpentinization of olivine (Frost et al. 2008). Aluminum and Ca mobility in the compact rock was limited, which only allowed for limited formation of chlorite from nearby serpentine (rxn. 3). Consequently, released Al predominantly had to be incorporated into the Ca bearing phases, ultimately favoring the formation of grossular and prehnite. Then again, the powder sample used in our experiments initially had an open pore space facilitating a significant increase of elemental mobility. This would enable ubiquitous formation of chlorite in association with olivine, and the Al fraction released upon desilication of plagioclase did not necessarily have to be incorporated in the forming Ca-bearing mineral phases. Xonotlite formed instead of prehnite or grossular, but it can equally be seen as a product of desilication of anorthite exhibiting an increased Ca/Si ratio of 1 (rxn. 5, 6, 7 and 12). Xonotlite was repeatedly reported in rodingitization associated mineral assemblages (O'Brien 1973; Esteban et al. 2003) and even in context of an altered troctolite (Capedri et al. 1980). The fact that no Ca-bearing phase exhibiting an intermediate Ca/Si ratio was observed among the solids retrieved form the 300 °C experiment might be attributable to the separation into domains of very high (δ and ε) and distinctly low Ca activities (α and β) through the pronounced mass transfer of Ca after a chemical potential gradient established between very differently buffered portions of the solids. In addition, comprehensive cementation of the outer portions limited dilution of the inner intergranular fluid and further plagioclase reaction eventually pushed local saturation over the threshold

for xonotlite formation. Once the first crystals had formed in the inner domains, they enabled further xonotlite precipitation even at lower Ca levels. This made domains δ and ε a sink for Ca and would arguably have facilitated further inward directed mass transfer of Ca^{2+} ions counterbalanced by an outflux of Mg^{2+} ions (see supplemental Fig. S4.2).

A major difference between the two experiments is the lack of brucite and the stability of olivine at 400 °C. Silica activity set by the serpentine-brucite buffer at 300 °C is much lower than that of the forsterite-serpentine assemblage at 400 °C (compare Figs. 7 and 8). If silica activity is sufficiently high, talc is expected to form like in altered troctolites exposed near the Kairei hydrothermal field (Nakamura et al. 2009), but not in our 400 °C experiment. In contrast to the compact rock in the natural system, increased Ca availability was not restricted to the immediate vicinity of reacting plagioclase in the experiment, and at higher log (aCa^{2+}/a^2H^+) values diopside is the stable high silica mineral phase. A similar explanation can account for the absence of tremolite. Also, similar to the troctolites investigated by Nakamura et al. (2009), grossular was confirmed as a product mineral, indicating low silica activities. Solids retrieved from the 400 °C experiment revealed that strong chemical contrasts prevailed between portions of the reactants where plagioclase was fully reacted and more isolated portions with unreacted plagioclase. This facilitated inward directed mass transfer of Ca and Al, counterbalanced by Mg and resulted in the development of chemically extremely variable microenvironments. Grossular and even xonotlite could form in context of further desilication of plagioclase in one space, while simultaneously clinopyroxene formed elsewhere. The exact formation mechanism of andradite in association with clinopyroxene remains unclear; however, the co-occurrence

677 of the two phases in context of high temperature serpentinization was reported before (Frost
678 1985).

679 Another peculiarity in the 400 °C experiment is the massive occurrence of almost
680 pure clinopyroxene ±andradite at the fluid-rock interface (see Fig. 5 D). Similar
681 occurrences of diopsidite were previously reported as an unusual type of dyke lithology in
682 the mantle section of the Oman ophiolite (Python and Ceuleneer 2003; Python et al. 2007).
683 These authors suggested a formation hypothesis in which seawater penetrated into the
684 upper mantle through cracks and fissures in the crust. The recharging fluids supposedly
685 reacted with plagioclase-rich lithologies in the crust and became enriched in Ca before they
686 penetrated into the mantle, where they caused diopsidite formation at extremely high
687 temperatures (>800 °C). The paragenetic association also included forsterite and anorthite.
688 The high temperature estimate was based on the co-occurrence of plagioclase, anorthite
689 and olivine and the anhydrous nature of this assemblage. The dykes always occurred close
690 to the former crust mantle transition zone and in particular in mantle sections that where
691 intensely percolated by hot primitive melts. Moreover, it was suggested that the heat
692 required for initiating and maintaining fluid circulation is provided by the crystallization
693 of nearby troctolites. Considering this close association with troctolites and an alteration
694 texture typical for rodingitization, massive occurrence of clinopyroxene in the 400 °C
695 experiment might provide an alternative low T formation hypothesis for this unique dyke
696 lithology. Secondary clinopyroxene in association with altered troctolites has been reported
697 before at Hess Deep where it was interpreted as a late high-grade (>360 °C) hydrothermal
698 overprint of a preceding chlorite-prehnite alteration that occurred lower temperatures (200
699 °C - Gillis et al. 2014; McCaig et al. 2018).

This is the peer-reviewed, final accepted version for American Mineralogist, published by the Mineralogical Society of America.
The published version is subject to change. Cite as Authors (Year) Title. American Mineralogist, in press.
DOI: https://doi.org/10.2138/am-2021-7832. http://www.minsocam.org/

Potential for H_2 production

Following an early complete reaction of plagioclase, further olivine reaction in the outer domains α and β produced predominantly Mg-rich serpentine and brucite (only α) in the 300 °C experiment. The Fe component of olivine reactant was oxidized to magnetite by water, releasing fairly large amounts of H_2 (up to 20 mM). The total extends of magnetite, and hence H_2 formation, were likely increased through additional Mg and Fe sourced from other portions of the solids. Andradite observed at the solid-fluid interface (gold cell contact) served as an additional, likely subordinate source of H_2. This observation could be seen as an analogue for massive andradite in veins associated with Ca-metasomatic alteration in lherzolite rocks described by Plümper et al. (2014) as an elevated W/R can be assumed for both environments. Plümper et al. (2014) proposed a reaction mechanism, in which the principle serpentinization related Fe-component magnetite was destabilized through the addition of Ca (rxn. 13).

$$4.5\ Mg_3Si_2O_5(OH)_4 + 9\ Ca^{2+} + 14\ H_2O\ +\ 2\ Fe_3O_4 \rightarrow\ 3\ Ca_3Fe_2Si_3O_{12} + 13.5\ Mg(OH)_2 +\ 18\ H^+ +\ H_2(aq) \qquad \text{rxn. 13}$$

As the final H_2 concentration could not be measured due to the premature cooling of the system, we calculated a hypothetical value based on the quantified amount of magnetite and andradite in the 300 °C experiment (45 mmol L^{-1}; according to rxn. 8 and 11) and compared it with an extrapolation based on the trend set through the previous fluid samples (30 mmol L^{-1}). The deviation could in part be subjected to a considerable error of the AGFM based quantification of magnetite. Additional CH_4 detected within the fluids is negligible in comparisson and a Sabatier type reaction does not provide a satisfying

720 explanation for the observed difference (McCollom and Seewald 2007; Bradley and
721 Summons 2010). Both H_2 estimates demonstrated a great potential for H_2 production in
722 context of alteration of olivine-rich troctolite.

723 At 400 °C, serpentinization of thermodynamically stable olivine was limited and
724 clinopyroxene formed in context of higher silica activities. Serpentine presence was
725 limited and abundant chlorite had similar Fe fractions as primary olivine. With Fe-rich
726 clinopyroxene and chlorite (±serpentine) there was little excess Fe available for the
727 formation of additional magnetite. However, chlorite always co-occurred with serpentine
728 and given that the thermodynamic model predicted a relatively large cronstedtite
729 component at 400 °C, considerable portions of the Fe-serpentine could be present in the
730 serpentine-chlorite mixture. Trivalent Fe incorporated in cronstedtite offers another H_2
731 formation pathway (Klein et al. 2013). Magnetite was barely observed, yet a significant
732 contribution of andradite (less Fe-rich than at 300 °C) represents a potential source for H_2
733 production (see rxn. 11 and 13). Balancing the amount of H_2 produced though andradite
734 and magnetite formation yields a potential concentration of 9 mM. However, subsequent
735 to the measured initial increase, H_2 was depleted from the reaction fluid at 400 °C. Methane
736 levels where somewhat higher than in the 300 °C experiment, but methane also became
737 depleted with progressing reaction. Falling H_2 and CH_4 concentrations after an initial
738 increase imply a yet unidentified process that consumes the two components.

739 **IMPLICATIONS**

740 The results presented herein provide an initial experimental perspective on the
741 alteration mechanisms controlling the alteration of olivine-rich troctolites. The
742 observations confirm that first-order controls on the alteration process are defined by the

743 combined effects of olivine serpentinization and plagioclase desilication reactions (Frost
744 et al., 2008). Secondly, silica activity is key in determining the actual product mineral
745 assemblage and it is set either to a relatively low (serpentine-brucite) or high (serpentine-
746 forsterite) level depending on alteration temperature. The experiments also highlight how
747 variable reaction rates in portions of a reacting rock that are closer or further away from a
748 solid-fluid interface can produce stark contrasts in local buffering of the water-rock
749 reaction and that this can entail pronounced selective mass transfer along chemical
750 potential gradients. Progressive pervasive cementation by secondary phases like
751 serpentine, chlorite, acicular clinopyroxene and xonotlite can increase partial isolation of
752 certain rock portions, further increasing the tension between differently buffered portions
753 of the solids. A selective diffusional mass transfer (Ca + Al counterbalanced by Mg and,
754 to a lesser extent, Fe) enables the development of chemically extreme microenvironments
755 that allow for the abundant formation of phases like magnetite, andradite, grossular or
756 xonotlite that would not form in entirely equilibrated systems. The magnetite and andradite
757 formation associated oxidation of iron mediates a significant H_2 production that can sustain
758 chemosynthesis based microbial communities, especially at temperatures where brucite is
759 stable (<315-340 °C). As the composition of troctolites closely resembles the chemistry of
760 komatiites, their alteration could also be a good analogue for komatiite serpentinization
761 processes that might have played a crucial role as an energy source for early life on earth
762 (Kumagai et al. 2008; Nakamura et al. 2009). While H_2 production is limited at the higher
763 temperature level, the observation that more CH_4 is formed and both compounds are
764 eventually depleted from the fluid implies a further conversion to different, possibly
765 organic components that should be further investigated. The described massive occurrence

of clinopyroxene association with minor andradite along a fluid-solid interface at the higher temperature level resembles a massive diopsidite in dykes found in the Oman ophiolite (Python et al., 2007). The serpentinization of olivine-rich troctolite might provide an alternative formation scenario for these peculiar lithologies that does not require nearly as high temperatures as previously suggested.

Whereas this study focuses on olivine-rich troctolites, more plagioclase-rich troctolites are also a common rock type, both in the oceanic lower crust of fast- (e.g., Gillis et al., 2014) and slow-spreading ridges (e.g., Dick et al., 2008) as well as in association with anorthosite intrusions (Drüppel 2003). Considering the documented strong interdependence of the olivine and plagioclase reactions, a shift towards a more plagioclase-rich lithology would certainly have a profound impact on the alteration process. In particular at elevated temperatures (>350 °C), a more prominent plagioclase reaction could facilitate an increased co-reaction of otherwise stable olivine including the oxidation of its fayalite component and thereby increase the potential for H_2 formation. This could be further explored in future experimental studies. In addition, more emphasis should be put on investigating the impact of variable element mobility during rock alteration as the experiments demonstrated how major deviations in this regard can arise from reacting a compact rock compared to powder sample.

Acknowledgements

This study was in part funded by the DFG Koselleck project grant BA 1605/10-1. Additional funding was provided by the Deutsche Forschungsgemeinschaft (DFG, German Research Foundation) under Germany´s Excellence Strategy – EXC-2077 – 390741603. Funding for the hydrothermal apparatus was provided by a MARUM Incentive fund to

W.B. Many thanks go to B. Bieseler for keeping company during night shifts at the microprobe and for fruitful discussions. We also thank P. Monien and Silvana Pape for help with ICP-MS and ICP-OES measurements. We are grateful to M. Wendschuh, P. Witte, T. Frederichs and D. Muir for their support with XRD / TG, SEM and AGFM analyses. We also thank Andrew McCaig, Bruce Yardley and two anonymous reviewers that helped to improve earlier versions of this manuscript.

References cited

Albers, E., Bach, W., Klein, F., Menzies, C.D., Lucassen, F., and Teagle, D.A.H. (2019) Fluid-rock interactions in the shallow Mariana forearc: Carbon cycling and redox conditions. Solid Earth, 10, 907–930.

Bach, W., and Klein, F. (2008) The petrology of seafloor rodingites: Insights from geochemical reaction path modeling. Lithos, 112, 103–117.

Beard, J.S., Frost, B.R., Fryer, P., McCaig, a., Searle, R., Ildefonse, B., Zinin, P., and Sharma, S.K. (2009) Onset and Progression of Serpentinization and Magnetite Formation in Olivine-rich Troctolite from IODP Hole U1309D. Journal of Petrology, 50, 387–403.

Bethke, C.M. (2005) The Geochemists Workbench®, version 6.0, GWB Essentials Guide, 76 p.

Blackman, D.K., Cann, J.R., Janssen, B., and Smith, D.K. (1998) Origin of extensional core complexes: Evidence from the Mid-Atlantic Ridge at Atlantis Fracture Zone. Journal of Geophysical Research, 103, 21315.

Blackman, D.K., Ildefonse, B., John, B.E., Ohara, Y., Miller, D.J., Abe, N., Abratis, M.W.,

Andal, E.S., Andréani, M., Awaji, S., and others (2011) Drilling constraints on lithospheric accretion and evolution at Atlantis Massif, Mid-Atlantic Ridge 30°N. Journal of Geophysical Research, 116, B07103.

Blanc, P., Bourbon, X., Lassin, a., and Gaucher, E.C. (2010) Chemical model for cement-based materials: Temperature dependence of thermodynamic functions for nanocrystalline and crystalline C-S-H phases. Cement and Concrete Research, 40, 851–866.

Bradley, A.S., and Summons, R.E. (2010) Multiple origins of methane at the Lost City Hydrothermal Field. Earth and Planetary Science Letters, 297, 34–41.

Cannat, M., Fontaine, F., and Escartín, J. (2010) Serpentinization and Associated Hydrogen And Methane Fluxes at Slow Spreading Ridges. Geophysical Monograph, 188, 241–264.

Capedri, S., Venturelli, G., Bocchi, G., Dostal, J., Garuti, G., Rossi, A., Modena, U., Parma, U., and Bologna, U. (1980) Contributions to Mineralogy and The Geochemistry and Petrogenesis of an Ophiolitic Sequence From Pindos , Greece. Contributions to Mineralogy and Petrology, 189500, 189–200.

Charlou, J.L., Donval, J.P., Fouquet, Y., Jean-Baptiste, P., and Holm, N. (2002) Geochemistry of high H2 and CH4 vent fluids issuing from ultramafic rocks at the Rainbow hydrothermal field (36°14'N, MAR). Chemical Geology, 191, 345–359.

Dick, H.J.B., Tivey, M. a., and Tucholke, B.E. (2008) Plutonic foundation of a slow-spreading ridge segment: Oceanic core complex at Kane Megamullion, 23°30′N, 45°20′W. Geochemistry Geophysics Geosystems, 9, n/a-n/a.

833 Dickson, F.W., Blount, C.W., and Tunell, G. (1963) Use of hydrothermal solution
834 equipment to determine the solubility of anhydrate in water from 100 °C to 275 °C
835 and from 1 bar to 1000 bars pressure. American Journal of Science, 261, 61–78.

836 Drouin, M., Godard, M., Ildefonse, B., Bruguier, O., and Garrido, C.J. (2009) Geochemical
837 and petrographic evidence for magmatic impregnation in the oceanic lithosphere at
838 Atlantis Massif, Mid-Atlantic Ridge (IODP Hole U1309D, 30°N). Chemical Geology,
839 264, 71–88.

840 Drouin, M., Ildefonse, B., and Godard, M. (2010) A microstructural imprint of melt
841 impregnation in slow spreading lithosphere: Olivine-rich troctolites from the Atlantis
842 Massif, Mid-Atlantic Ridge, 30°N, IODP Hole U1309D. Geochemistry, Geophysics,
843 Geosystems, 11, n/a-n/a.

844 Esteban, J.J., Cuevas, J., and Tubia, M.J. (2003) Xonotlite in rodingite assemblages from
845 the Ronda peridotites, Betic Cordilleras, southern Spain. The Canadian Mineralogist,
846 41, 161–170.

847 Flanders, P.J. (1988) An alternating-gradient magnetometer (invited). Journal of Applied
848 Physics, 63, 3940.

849 Földvári, M. (2011) Handbook of the thermogravimetric system of minerals and its use in
850 geological practice, 1–179 p. Central European Geology Vol. 56.

851 Frost, B.R. (1985) On the stability of sulfides, oxides, and native metals in serpentinite.
852 Journal of Petrology, 26, 31–63.

853 Frost, B.R., and Beard, J.S. (2007) On Silica Activity and Serpentinization. Journal of
854 Petrology, 48, 1351–1368.

855 Frost, B.R., Beard, J.S., McCaig, a., and Condliffe, E. (2008) The Formation of Micro-
856 Rodingites from IODP Hole U1309D: Key To Understanding the Process of
857 Serpentinization. Journal of Petrology, 49, 1579–1588.

858 German, C.R., Bowen, a, Coleman, M.L., Honig, D.L., Huber, J. a, Jakuba, M. V, Kinsey,
859 J.C., Kurz, M.D., Leroy, S., McDermott, J.M., and others (2010) Diverse styles of
860 submarine venting on the ultraslow spreading Mid-Cayman Rise. Proceedings of the
861 National Academy of Sciences of the United States of America, 107, 14020–5.

862 Gillis, K.M., Snow, J.E., Klaus, A., Guerin, G., Abe, N., Akizawa, N., Ceuleneer, G.,
863 Cheadle, M.J., Adrião, Á., Faak, K., and others (2014) Hess Deep Plutonic Crust:
864 Exploring the Plutonic Crust at a Fast-Spreading Ridge: New Drilling at Hess Deep.
865 Proceedings of the Ocean Drilling Program, 345.

866 Ildefonse, B., Blackman, D., John, E., Barbara, O., Yasuhiko, M., Jay, D., MacLeod, J.,
867 and Christopher, I.E. 304-305 S. (2006) IODP Expedition 304 & 305
868 Characterize the Lithology, Structure, and Alteration of an Oceanic Core Complex.
869 Scientific Drilling, 4–11.

870 Johnson, J.W., Oelkers, E.H., and Helgeson, H.C. (1992) SUPCRT92: A software package
871 for calculating the standard molal thermodynamic properties of minerals, gases,
872 aqueous species, and reactions from 1 to 5000 bar and 0 to 1000°C. Computers &
873 Geosciences, 18, 899–947.

874 Jöns, N., Bach, W., and Klein, F. (2010) Magmatic influence on reaction paths and element
875 transport during serpentinization. Chemical Geology, 274, 196–211.

876 Klein, F., Bach, W., Jöns, N., McCollom, T., Moskowitz, B., and Berquó, T. (2009) Iron

877 partitioning and hydrogen generation during serpentinization of abyssal peridotites
878 from 15°N on the Mid-Atlantic Ridge. Geochimica et Cosmochimica Acta, 73, 6868–
879 6893.

880 Klein, F., Bach, W., and McCollom, T.M. (2013) Compositional controls on hydrogen
881 generation during serpentinization of ultramafic rocks. Lithos, 178, 55–69.

882 Klein, F., Bach, W., Humphris, S.E., Kahl, W.-A., Jons, N., Moskowitz, B., and Berquo,
883 T.S. (2014) Magnetite in seafloor serpentinite--Some like it hot. Geology, 42, 135–
884 138.

885 Konn, C., Charlou, J.L., Holm, N.G., and Mousis, O. (2015) The Production of Methane,
886 Hydrogen, and Organic Compounds in Ultramafic-Hosted Hydrothermal Vents of the
887 Mid-Atlantic Ridge. Astrobiology, 15, 381–399.

888 Kumagai, H., Nakamura, K., Toki, T., Morishita, T., Okino, K., Ishibashi, J.I., Tsunogai,
889 U., Kawagucci, S., Gamo, T., Shibuya, T., and others (2008) Geological background
890 of the Kairei and Edmond hydrothermal fields along the Central Indian Ridge:
891 Implications of their vent fluids'distinct chemistry. Geofluids, 8, 239–251.

892 McCaig, A.M., Titarenko, S.S., Savov, I.P., Cliff, R.A., Banks, D., Boyce, A., and
893 Agostini, S. (2018) No significant boron in the hydrated mantle of most subducting
894 slabs. Nature Communications, 9.

895 McCollom, T.M., and Bach, W. (2009) Thermodynamic constraints on hydrogen
896 generation during serpentinization of ultramafic rocks. Geochimica et Cosmochimica
897 Acta, 73, 856–875.

898 McCollom, T.M., and Seewald, J.S. (2007) Abiotic Synthesis of Organic Compounds in

899 Deep-Sea Hydrothermal Environments. Chemical Reviews, 107, 382–401.

900 Nakamura, K., Morishita, T., Bach, W., Klein, F., Hara, K., Okino, K., Takai, K., and
901 Kumagai, H. (2009) Serpentinized troctolites exposed near the Kairei Hydrothermal
902 Field, Central Indian Ridge: Insights into the origin of the Kairei hydrothermal fluid
903 supporting a unique microbial ecosystem. Earth and Planetary Science Letters, 280,
904 128–136.

905 Nozaka, T., Wintsch, R.P., and Meyer, R. (2017) Serpentinization of olivine in troctolites
906 and olivine gabbros from the Hess Deep Rift. Lithos, 282–283, 201–214.

907 O'Brien, J.P. (1973) Xonotlite and Rodingites from Wairere, New Zealand. Mineralogical
908 Magazine, 39, 233–240.

909 Plümper, O., Beinlich, A., Bach, W., Janots, E., and Austrheim, H. (2014) Garnets within
910 geode-like serpentinite veins: Implications for element transport, hydrogen
911 production and life-supporting environment formation. Geochimica et Cosmochimica
912 Acta, 141, 454–471.

913 Proskurowski, G., Lilley, M.D., Kelley, D.S., and Olson, E.J. (2006) Low temperature
914 volatile production at the Lost City Hydrothermal Field, evidence from a hydrogen
915 stable isotope geothermometer. Chemical Geology, 229, 331–343.

916 Python, M., and Ceuleneer, G. (2003) Nature and distribution of dykes and related melt
917 migration structures in the mantle section of the Oman ophiolite. Geochemistry,
918 Geophysics, Geosystems, 4, n/a-n/a.

919 Python, M., Ceuleneer, G., Ishida, Y., Barrat, J.-A., and Arai, S. (2007) Oman diopsidites:
920 a new lithology diagnostic of very high temperature hydrothermal circulation in

921 mantle peridotite below oceanic spreading centres. Earth and Planetary Science
922 Letters, 255, 289–305.

923 Renna, M.R., and Tribuzio, R. (2011) Olivine-rich Troctolites from Ligurian Ophiolites
924 (Italy): Evidence for Impregnation of Replacive Mantle Conduits by MORB-type
925 Melts. Journal of Petrology, 52, 1763–1790.

926 Sanfilippo, A., and Tribuzio, R. (2013) Origin of olivine-rich troctolites from the oceanic
927 lithoshere: a comparison between the alpine jurassic ophiolites and modern slow
928 spreading ridges. Ofioliti, 38, 89–99.

929 Sanfilippo, A., Dick, H.J.B., and Ohara, Y. (2013) Melt-rock reaction in the mantle: Mantle
930 troctolites from the parecevela ancient back-arc spreading center. Journal of
931 Petrology, 54, 861–885.

932 Schmidt, K., Koschinsky, a, Garbeschonberg, D., Decarvalho, L., and Seifert, R. (2007)
933 Geochemistry of hydrothermal fluids from the ultramafic-hosted Logatchev
934 hydrothermal field, 15°N on the Mid-Atlantic Ridge: Temporal and spatial
935 investigation. Chemical Geology, 242, 1–21.

936 Seyfried, W.E., Janecky, D.R., and Berndt, M.E. (1987) Rocking autoclaves for
937 hydrothermal experiments. II. The flexible reaction-cell system. In Hydrothermal
938 Experimental Techniques pp. 216–239. Wiley-Interscience Publications.

939 Seyfried, W.E., Foustoukos, D.I., and Fu, Q. (2007) Redox evolution and mass transfer
940 during serpentinization: An experimental and theoretical study at 200°C, 500bar with
941 implications for ultramafic-hosted hydrothermal systems at Mid-Ocean Ridges.
942 Geochimica et Cosmochimica Acta, 71, 3872–3886.

943 Sleep, N.H., Meibom, a, Fridriksson, T., Coleman, R.G., and Bird, D.K. (2004) H2-rich
944 fluids from serpentinization: geochemical and biotic implications. Proceedings of the
945 National Academy of Sciences of the United States of America, 101, 12818–12823.

946 Smith, D., Escartín, J., Schouten, H., and Cann, J. (2012) Active long-lived faults emerging
947 along slow-spreading mid-ocean ridges. Oceanography, 25, 94–99.

948 Smith, D.K., Escartín, J., Schouten, H., and Cann, J.R. (2008) Fault rotation and core
949 complex formation: Significant processes in seafloor formation at slow-spreading
950 mid-ocean ridges (Mid-Atlantic Ridge, 13°-15°N). Geochemistry, Geophysics,
951 Geosystems, 9, n/a-n/a.

952 Suhr, G., Hellebrand, E., Johnson, K., and Brunelli, D. (2008) Stacked gabbro units and
953 intervening mantle: A detailed look at a section of IODP Leg 305, Hole U1309D.
954 Geochemistry, Geophysics, Geosystems, 9, n/a-n/a.

955 Takai, K., Gamo, T., Tsunogai, U., Nakayama, N., Hirayama, H., Nealson, K., and
956 Horikoshi, K. (2004) Geochemical and microbiological evidence for a hydrogen-
957 based, hyperthermophilic subsurface lithoautotrophic microbial ecosystem
958 (HyperSLiME) beneath an active deep-sea hydrothermal field. Extremophiles, 8,
959 269–282.

960 Trittschack, R., Grobéty, B., and Brodard, P. (2014) Kinetics of the chrysotile and brucite
961 dehydroxylation reaction: A combined non-isothermal/isothermal thermogravimetric
962 analysis and high-temperature X-ray powder diffraction study. Physics and Chemistry
963 of Minerals, 41, 197–214.

964 Wolery, T.J. (1992) EQ3/6 - A Software Package for Geochemical Modeling of Aqueous

965 Systems : Package Overview and Installation Guide (Version 7.0). Lawrence
966 Livermore National Laboratory.

967 Wolery, T.J., and Jove-Colon, C.-F. (2004) Qualification of Thermodynamic Data for
968 Geochemical Modeling of Mineral-Water Interactions in Dilute Systems. Interactions,
969 1–212.

970

971 **Figure captions**

972 **Figure 1:** Summary of solid phase alteration modes retrieved from the conducted
973 experiments. Formation of alteration phases like serpentine, chlorite, clinopyroxene and
974 xonotlite facilitated a pervasive cementation. As a result of variable degrees of isolation
975 distinct mineral assemblages occur in different microenvironments. Five domains (α, β, γ,
976 δ, ε) could be distinguished in the solids retrieved from the 300 °C run, whereas 4 distinct
977 assemblages (α*, β*, γ*, δ*) where identified in the concretion produced in the 400 °C run.
978 References given in rectangular brackets for the investigated gold cell contacts indicate the
979 domains which can be associated with these contact surface assemblages. The ranking
980 position of olivine attributed with an asterisk takes into account that the mineral was in part
981 plucked out from the respective domains during mount preparation. Details complementing
982 this summary of different mineral phases are provided in the text and in Fig. 3 and 5, which
983 cover a close up of profile sections S and S*.

984 **Figure 2:** Measured evolving fluid composition in the experiments. **(A)** in the 300 °C run
985 and **(B)** in the 400 °C experiment.

Figure 3: Retrieved mineral assemblage from the 300 °C experiment I. **(A+B)** SEM element mapping (Mg, Al, Fe, Ca) of profile section S (see Fig. 1) and a corresponding false color image contrasting identified mineral phases. From top to bottom section S covers 5 (α, β, γ, δ, ε) domains in a zonation of distinct mineral assemblages distinguished in the 300 °C run. **(C)** BSE image of upper part of the cemented mass comprised of a fine serpentine-chlorite mixture, andradite crystals and relict olivine. **(D)** BSE image of the mineral assemblage in domain α. Patches of brucite intergrown with a fine serpentine-chlorite mixture. Chlorite is concentrated in a thin rim marking the boundary to cavities in the texture. Relict olivine with dissolution features that probably filled most of the cavities in the unpolished mount, is visible in the center of some cavities. **(E)** BSE image showing the occurrence of magnetite in domain α and β. **(F)** Schematic drawing of the solid reactants within the gold reaction cell. Arrows indicate elemental transfer between the top and bottom domains. **(G)** BSE image of the lower part of the cemented mass, which is mostly comprised of a chlorite-serpentine mixture and xonotlite. **(H)** BSE image of xonotlite void fill and thick chlorite coronas around dissolved crystals of olivine in domain δ. **(I)** Large portions of unreacted anorthite in domain ε. Remnants of unreacted olivine with thick chlorite rims and xonotlite in the interstitials.

Figure 4: Compositional variability in serpentine and serpentine-chlorite mixtures. Serpentine from the outermost domain α (300 °C) exhibits an almost pure magnesian end-member composition with minor additions of Fe. While serpentine contributions to chlorite (300 and 400 °C experiment) are not identifiable by optical measures, reduced Al fractions clearly indicate its additional presence. A significant amesite component is not indicated.

1008 **Figure 5:** Retrieved mineral assemblage from the 400 °C experiment. **(A+B)** SEM element
1009 mapping (Al, Fe, Ca) of profile section S* (see Fig. 1) and a corresponding false color
1010 image contrasting identified mineral phases. From top to bottom section S* covers 4 (α*,
1011 β*, γ*, δ*) domains in a zonation of distinct mineral assemblages distinguished for the 400
1012 °C run. The elemental transfer between the top and bottom domains within the cell is
1013 indicated. **(C)** BSE image of void clinopyroxene in domain α* and β*. Andradite-rich
1014 garnet occurs in a typical dense aggregation of small isometric crystals associated with
1015 clinopyroxene. **(D)** BSE images of the crust surface that represents the solid-gold cell
1016 contact. The upper part of the crust consists of massive clinopyroxene and associated
1017 andradite crystals. The lower part of the crust is almost exclusively comprised of chlorite,
1018 with some grossular-rich garnet and minor xonotlite. **(E)** BSE image of the transition
1019 between domains γ* and δ*. Thick, fine-grained chlorite completely replaced primary
1020 olivine, whereas the interstitials are filled with fibrous xonotlite and grossular-rich garnet.
1021 Larger fractions of anorthite remained unreacted in domain δ*.

1022 **Figure 6:** Predicted equilibrium phase assemblages as plagioclase and olivine are
1023 successively added to water. $\xi = 1$ represents the proportions of fluid to solids used in the
1024 experiment. The vertical lines represent the observed reaction turnover. See text for details
1025 on the calculations. **(A)** Reaction path model for the 300 °C experiment. Antigorite,
1026 monticellite, tremolite, amesite, diopside, garnet, akermanite, merwinite, wollastonite and
1027 portlandite were suppressed from the model. **(B)** Reaction path model for the 400 °C
1028 experiment. Antigorite, monticellite, tremolite, amesite, magnetite, hematite, wuestite and
1029 cronstedtite were suppressed from the model.

This is the peer-reviewed, final accepted version for American Mineralogist, published by the Mineralogical Society of America.
The published version is subject to change. Cite as Authors (Year) Title. American Mineralogist, in press.
DOI: https://doi.org/10.2138/am-2021-7832. http://www.minsocam.org/

Figure 7: Activity-activity diagrams showing the phase relations in the system MgO-SiO_2-H_2O (blue dashed lines) speciated over the phase relations in the system MgO-SiO_2-CaO-Al_2O_3-H_2O (red solid lines) at 300 °C and 50 MPa. Only minerals identified in the solids retrieved from the experiment were considered. Changing in-situ activity characteristics of the taken fluid samples (green stars) as well as the evolution of the corresponding titration model fluid (yellow path) are plotted for comparison. Phase relations of iron bearing phases that are key to potential H_2 production (green, pink and light blue dashed lines for H_2 activity of unity, 20 and 5 mmol L^{-1}) confirm that magnetite can be expected to form in the outer low Ca domains.

Figure 8: Activity-activity diagrams showing the phase relations in the system MgO-SiO_2-H_2O (blue dashed lines) speciated over the phase relations in the system MgO-SiO_2-CaO-Al_2O_3-H_2O (red solid lines) at 400 °C and 50 MPa. Only minerals identified in the solids retrieved from the experiment were considered. Changing in-situ activity characteristics of the taken fluid samples (green stars) as well as the evolution of the corresponding titration model fluid (yellow path) are plotted for comparison. Phase relations of iron bearing phases that are key to potential H_2 production (green and white dashed lines for H_2 activity of unity and 0.2 mmol L^{-1}) confirm that andradite instead of magnetite is the thermodynamically stable phase at moderately elevated Ca activities. Rxn. 10 is not shown as it would proceed throughout the depicted space.

This is the peer-reviewed, final accepted version for American Mineralogist, published by the Mineralogical Society of America.
The published version is subject to change. Cite as Authors (Year) Title. American Mineralogist, in press.
DOI: https://doi.org/10.2138/am-2021-7832. http://www.minsocam.org/

Table 1: Summary of fluid data and related modelling results. Concentrations of dissolved elements and gases are given in µmol/kg.

Sample	Time [h]	Description	m_{left} [g]	m_{taken} [g]	V_{left} [ml]	W/R	Mg	Al	Si	Ca	Na	$pH_{25°C}$	$pH_{in\text{-}situ}$	Salinity [wt.-%]	H_2	CH_4
						Experimental Run at 300°C and 40 MPa										
T1.0	0	Stock solution	54.2	-	53.1	3.3	25	0	5	0	537	5.90	-	3.0	-	-
T1.1	1	Initial cool	52.6	1.60	51.5	3.2	153	6	31	29	537	6.53	5.50*	3.0	1	0
T1.2	238	hot	49.4	3.15	48.4	3.0	14	1	34	2035	537	9.33	6.42	3.1	5222	12
T1.3	646	hot	46.1	3.32	45.2	2.8	4	1	9	1484	541	9.60	6.54	3.1	10164	17
T1.4	1174	hot	43.0	3.07	42.1	2.6	3	0	7	1184	546	10.33	7.24	3.2	20073	35
T1.5	1822	cool	39.8	3.22	39.0	2.4	24	0	0	1722	546	10.87	-	3.2	3090	9
						Experimental Run at 400°C and 40 MPa										
T2.0	0	Stock solution	54.3	-	53.3	3.3	25	0	5	0	537	5.90	-	3.0	-	
T2.1	1	Initial cool	52.7	1.65	51.7	3.2	153	8	31	19	520	6.74	6.14*	3.0	1	0
T2.2	238	hot	49.2	3.49	48.2	3.0	19	0	426	3472	563	5.95	6.16	3.1	3959	247
T2.3	646	hot	45.6	3.61	44.7	2.7	13	0	555	1822	546	5.87	6.17	3.2	1447	159
T2.4	1174	hot	42.3	3.26	41.5	2.5	7	0	796	1144	571	6.30	6.24	3.2	233	71
T2.5	1822	cool	39.1	3.19	38.3	2.4	127	0	163	1208	546	8.61	-	3.2	232	115

*Values were modelled analogue to those for samples taken at elevated temperatures for visual comparison.

This is the peer-reviewed, final accepted version for American Mineralogist, published by the Mineralogical Society of America.
The published version is subject to change. Cite as Authors (Year) Title. American Mineralogist, in press.
DOI: https://doi.org/10.2138/am-2021-7832. http://www.minsocam.org/

Table 2: Mineral chemistry for reactants and phases retrieved from the 300 °C experiment determined via EMP analyses.

Component	Olivine[1]	Plagioclase[2]	Serpentine[1]	Chlorite[1]	Brucite[1]	Xonotlite	*Olivine[1]	*Plagioclase[2]
Analysis	(15)	(5)	(9)	(8)	(5)	(10)	(14)	(5)
SiO_2	40.89	40.76	35.65	34.43	0.19	45.02	41.41	43.97
TiO_2	0.01	0.00	0.00	0.00	0.00	0.01	0.00	0.01
Al_2O_3	0.02	36.38	0.11	13.20	0.17	2.62	0.00	36.55
Cr_2O_3	0.01	0.00	0.00	0.02	0.00	0.00	0.00	0.01
FeO	8.85	0.58	1.42	5.44	8.42	0.60	9.14	0.46
MgO	49.86	0.07	34.46	31.31	64.43	0.07	49.62	0.08
MnO	0.15	0.02	0.06	0.10	0.41	0.04	0.14	0.01
CaO	0.07	18.09	0.01	0.31	0.01	44.82	0.03	19.44
Na_2O	0.01	0.43	0.04	0.07	0.00	0.04	0.00	0.43
K_2O	0.00	0.01	0.01	0.02	0.01	0.00	0.00	0.01
Total	99.87	96.36	71.77	84.91	73.63	93.23	100.35	100.99
Si	1.00	1.96	2.01	3.35	0.00	5.65	1.01	2.02
Ti	0.00	0.00	0.00	0.00	0.00	0.00	0.00	0.00
Al	0.00	2.06	0.01	1.51	0.00	0.39	0.00	1.98
Cr	0.00	0.00	0.00	0.00	0.00	0.00	0.00	0.00
Fe^{2+}	0.18	0.02	0.08	0.44	0.07	0.06	0.19	0.02
Mg	1.82	0.01	2.88	4.54	0.92	0.01	1.80	0.01
Mn^{2+}	0.00	0.00	0.00	0.01	0.00	0.00	0.00	0.00
Ca	0.00	0.93	0.00	0.03	0.00	6.03	0.00	0.96
Na	0.00	0.04	0.00	0.01	0.00	0.01	0.00	0.04
K	0.00	0.00	0.00	0.00	0.00	0.00	0.00	0.00
Basis (O)	4.00	8.00	7.00	14.00	1.00	18.00	4.00	8.00
[1]XMg [2]XCa	0.91	0.96	0.97	0.91	0.93		0.91	0.96

[1]XMg = Mg / (Mg + Fe) [2]XCa = Ca / (Ca + Na) *Initial characterization of the reactants

This is the peer-reviewed, final accepted version for American Mineralogist, published by the Mineralogical Society of America.
The published version is subject to change. Cite as Authors (Year) Title. American Mineralogist, in press.
DOI: https://doi.org/10.2138/am-2021-7832. http://www.minsocam.org/

Table 3: Mineral chemistry for phases retrieved from the 400 °C experiment determined via EMP analyses.

Component	Olivine[1]	Plagioclase[2]	Chlorite[1]	Clinopyroxene[1]	Xonotlite	Andradite[3]	Grossular[3]
Analysis	(12)	(5)	(28)	(14)	(2)	(6)	(11)
SiO_2	41.45	44.64	35.56	53.18	50.66	36.11	36.57
TiO_2	0.01	0.03	0.01	0.01	0.02	0.07	0.35
Al_2O_3	0.06	36.53	13.42	1.76	0.39	3.81	17.04
Cr_2O_3	0.01	0.01	0.01	0.00	0.01	0.00	0.01
FeO	9.24	0.61	5.28	4.53	1.25	22.18	7.07
MgO	49.89	0.08	32.58	15.22	0.52	0.84	1.17
MnO	0.15	0.00	0.06	0.18	0.20	0.08	0.16
CaO	0.07	19.44	0.11	25.31	46.33	33.59	35.38
Na_2O	0.00	0.52	0.05	0.08	0.00	0.02	0.02
K_2O	0.00	0.01	0.01	0.00	0.01	0.00	0.00
Total	101.27	101.91	87.36	100.36	99.42	96.72	97.77
Si	1.00	2.03	3.36	1.95	5.92	3.01	2.88
Ti	0.00	0.00	0.00	0.00	0.00	0.00	0.02
Al	0.00	1.96	1.49	0.08	0.05	0.37	1.58
Cr	0.00	0.00	0.00	0.00	0.00	0.00	0.00
Fe^{2+} *	0.17	0.02	0.42	0.14	0.14	1.54	0.47
Mg	1.81	0.01	4.59	0.83	0.10	0.10	0.14
Mn^{2+}	0.00	0.00	0.00	0.01	0.02	0.00	0.00
Ca	0.00	0.95	0.01	1.00	5.82	2.99	2.98
Na	0.00	0.05	0.01	0.01	0.00	0.00	0.00
K	0.00	0.00	0.00	0.00	0.00	0.00	0.00
Basis (O)	4.00	8.00	14.00	6.00	18.00	12.00	12.00
$^1X_{Mg}$ $^2X_{Ca}$ $^3X_{Fe}$	0.91	0.95	0.92	0.86		0.81	0.23

*Iron for andradite-grossular solid solutions was calculated as ferric Fe^{3+}

$^1X_{Mg}$ = Mg / (Mg + Fe) $^2X_{Ca}$ = Ca / (Ca + Na) $^3X_{Fe}$ = Fe / (Fe + Al)

This is the peer-reviewed, final accepted version for American Mineralogist, published by the Mineralogical Society of America.
The published version is subject to change. Cite as Authors (Year) Title. American Mineralogist, in press.
DOI: https://doi.org/10.2138/am-2021-7832. http://www.minsocam.org/

Table 4: Mineral proportions derived from TG, AGFM and regression modelling. Total mass percentage is based on a ratio of modelled total vs retrieved total mass.

Components	Idealized formula*	M* [g/mol]	m [g]	X [wt.-%]	n [mol]	RP X [wt.-%]**	RP n [mol]**	M [g/mol]	m [g]	X [wt.-%]	n [mol]	RP X [wt.-%]**	RP n [mol]**
		Experiment at 300 °C and 40 MPa						***Experiment at 300 °C and 40 MPa***					
Initial		TG + AGFM based reconstruction				Reaction path model		TG + AGFM based reconstruction				Reaction path model	
Olivine	Mg_2SiO_4	146.55	12.96	77.79	8.84E-02	77.79	8.84E-02	146.51	12.96	77.78	8.85E-02	77.78	8.85E-02
Plagioclase	$CaAl_2Si_2O_8$	278.57	3.70	22.21	1.33E-02	22.21	1.33E-02	278.39	3.70	22.22	1.33E-02	22.22	1.33E-02
Total			16.7	100.00					16.66	100.00			
Final													
Olivine	Mg_2SiO_4	146.55	3.01	16.25	2.05E-02	17.48	2.21E-02	146.51	8.11	45.87	5.54E-02	48.55	5.86E-02
Plagioclase	$CaAl_2Si_2O_8$	278.57	1.16	6.26	4.16E-03	5.03	3.34E-03	278.39	0.33	1.87	1.19E-03	6.68	4.24E-03
Andradite	$Ca_3Fe_2Si_3O_{12}$	508.17	0.03	0.15	5.51E-05	-	-	495.49	0.10	0.57	2.02E-04	0.10	3.51E-05
Xonotlite	$Ca_6Si_6O_{17}(OH)_2$	721.15	1.08	5.82	1.49E-03	6.12	1.57E-03	718.18	0.36	2.04	5.01E-04	-	-
Serpentine[1,2]	$Mg_3Si_2O_5(OH)_4$	279.63	6.37	34.41	2.28E-02	37.04	2.45E-02	-	-	-	-	4.41	2.79E-03
Chlorite[1]	$Mg_5Al_2Si_3O_{10}(OH)_8$	568.19	5.61	30.32	9.75E-03	30.36	9.76E-03	566.62	6.76	38.24	1.16E-02	29.32	8.93E-03
Brucite[3]	$Mg(OH)_2$	60.50	0.81	4.39	1.34E-02	0.81	2.47E-03	-	-	-	-	-	-
Magnetite[4]	Fe_3O_4	231.53	0.45	2.40	1.92E-03	3.16	2.52E-03	231.53	0.01	0.06	4.32E-05	-	-
Grossular	$Ca_3Al_2Si_3O_{12}$	-	-		-	-	-	465.50	0.09	0.51	1.93E-04	-	-
Diopside	$CaMgSi_2O_6$	-	-		-	-	-	221.37	1.64	9.28	7.41E-03	10.94	8.74E-03
Total			18.51	99.98					17.68	98.42			

*Exact compositions derived from EMP based WDS analyses were used in the regression algorithm

**Resulting mineral proportions for a reaction turnover of 77.49% (300 °C) and 52.23% (400 °C) by weight – model at 50 MPa

[1]Sum of serpentine and chlorite equals the fraction derived by TG

[2]Molar weight from the 300 °C run was used to calculate the mole equivalent for the model run

[3]Brucite fraction equals the amount derived by TG plus 1 wt.% dissolved fraction [4]Magnetite determined via AGFM

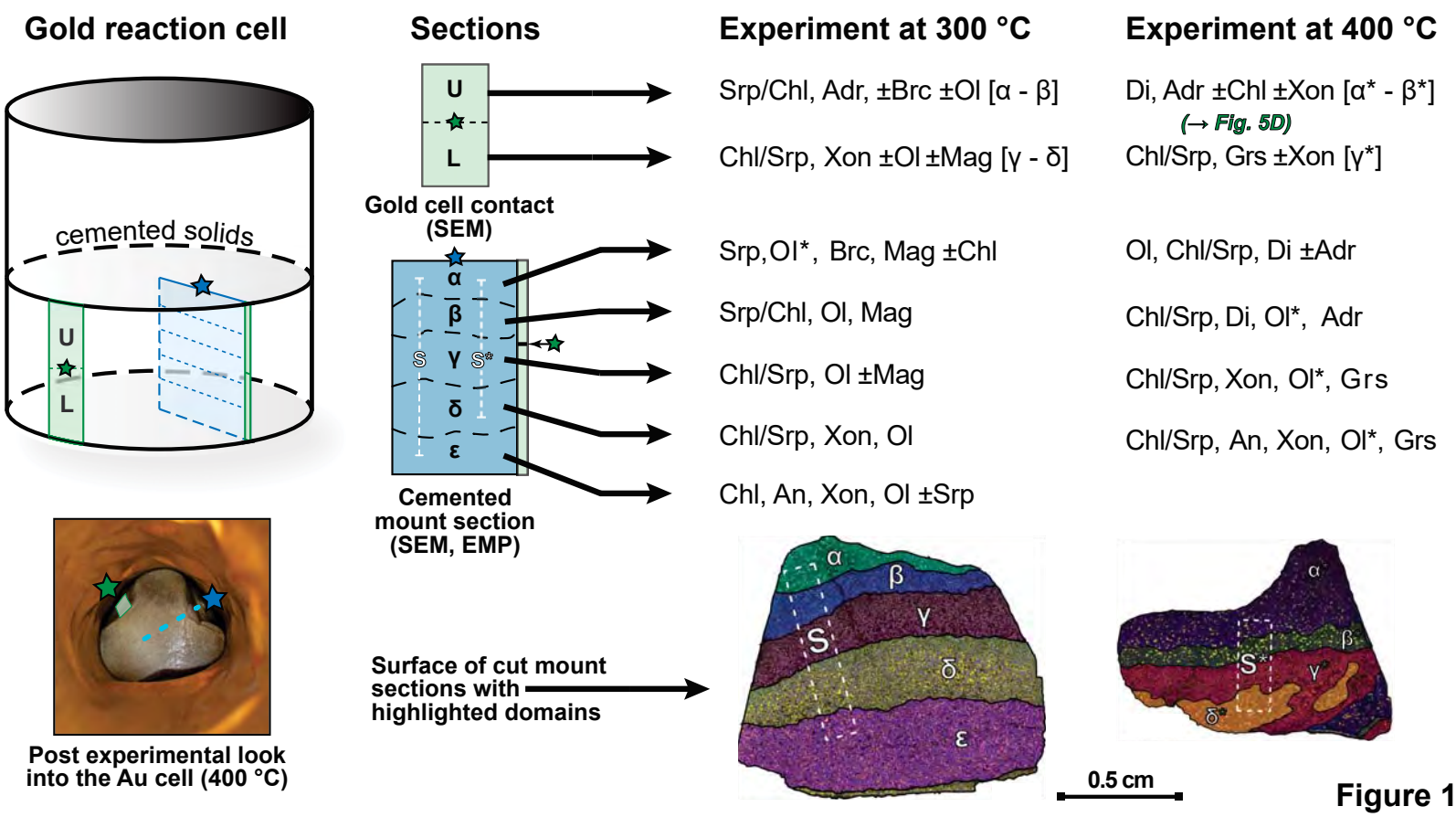
Gold reaction cell
Sections
Experiment at 300 °C
Experiment at 400 °C
cemented solids
U
L
Gold cell contact (SEM)
Srp/Chl, Adr, ±Brc ±Ol [α - β]
Chl/Srp, Xon ±Ol ±Mag [γ - δ]
Di, Adr ±Chl ±Xon [α* - β*]
(→ Fig. 5D)
Chl/Srp, Grs ±Xon [γ*]
α
β
γ
δ
ε
S
S*
Srp,Ol*, Brc, Mag ±Chl
Srp/Chl, Ol, Mag
Chl/Srp, Ol ±Mag
Chl/Srp, Xon, Ol
Chl, An, Xon, Ol ±Srp
Ol, Chl/Srp, Di ±Adr
Chl/Srp, Di, Ol*, Adr
Chl/Srp, Xon, Ol*, Grs
Chl/Srp, An, Xon, Ol*, Grs
Cemented mount section (SEM, EMP)
Post experimental look into the Au cell (400 °C)
Surface of cut mount sections with highlighted domains
0.5 cm

Figure 1

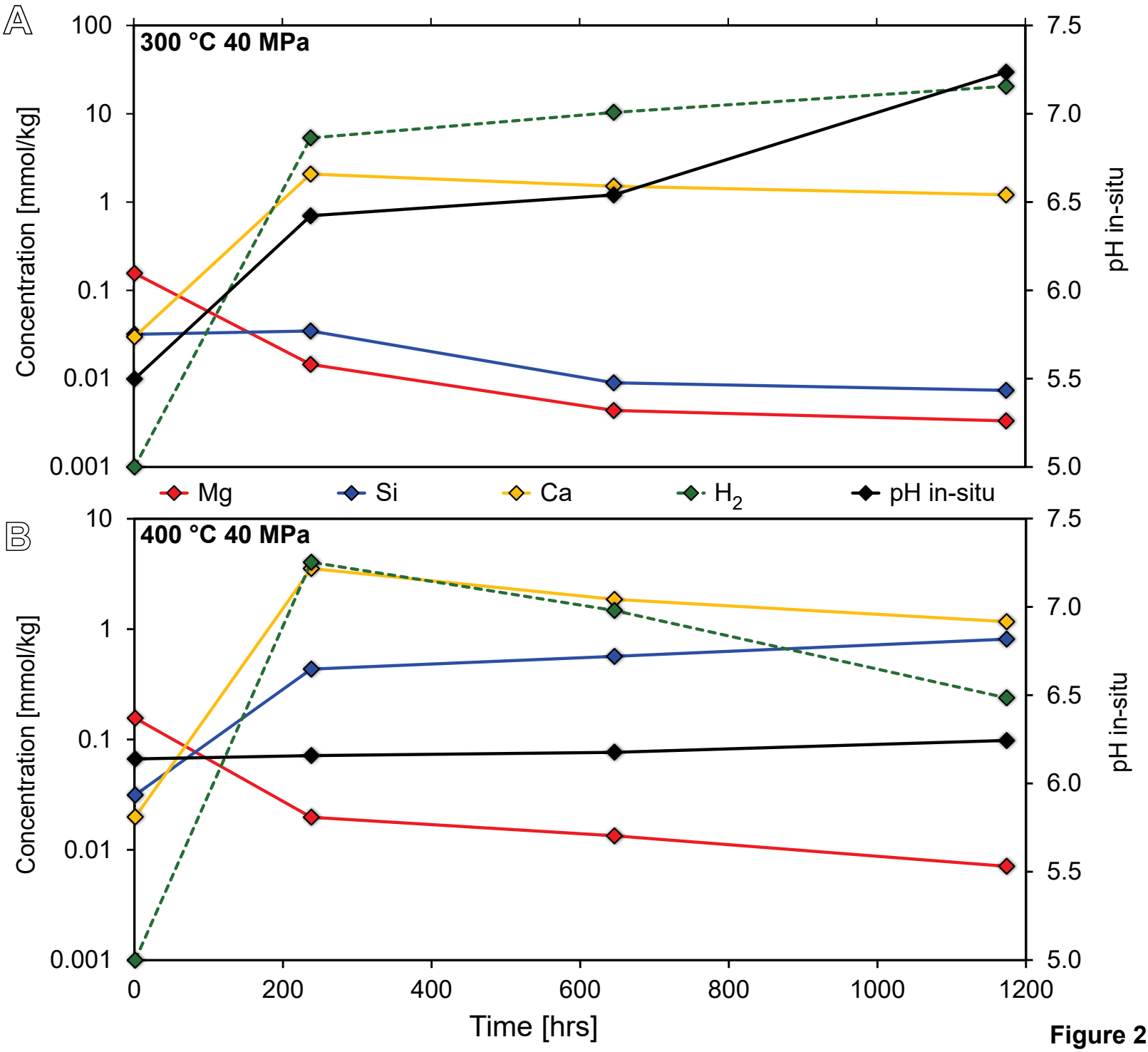
A
300 °C 40 MPa
Concentration [mmol/kg]
pH in-situ
100
10
1
0.1
0.01
0.001
7.5
7.0
6.5
6.0
5.5
5.0
Mg
Si
Ca
H2
pH in-situ
B
400 °C 40 MPa
Concentration [mmol/kg]
pH in-situ
10
1
0.1
0.01
0.001
7.5
7.0
6.5
6.0
5.5
5.0
0
200
400
600
800
1000
1200
Time [hrs]

Figure 2

A
α
β
γ
σ
ε
B
Top
Bottom
400 µm
Mg Al Fe Ca
C
upper rim
Adr
Srp/Chl
50 µm
D
α
Brc
Mag
Chl
Ol
Srp
Brc
75 µm
Mg↑↑, Fe↑, Ca+Al↓↓
E
β
Chl
Fe
Mag
Ol
Srp
25 µm
F
Diffusive fluid mixing
titanium cap
gold cell
bulk fluid
solids
well mixed
isolated
max. isolation
G
lower rim
Xon
Chl
Mag
100 µm
H
δ
Srp
Ol
Chl
Xon
25 µm
Ca+Al↑↑, Mg↓↓, Fe↓
ε
Xon
Ol
An
Chl
100 µm
Olivine
Serpentine
Brucite
Magnetite
Chlorite
Xonotlite
Plagioclase
Void
Figure 3

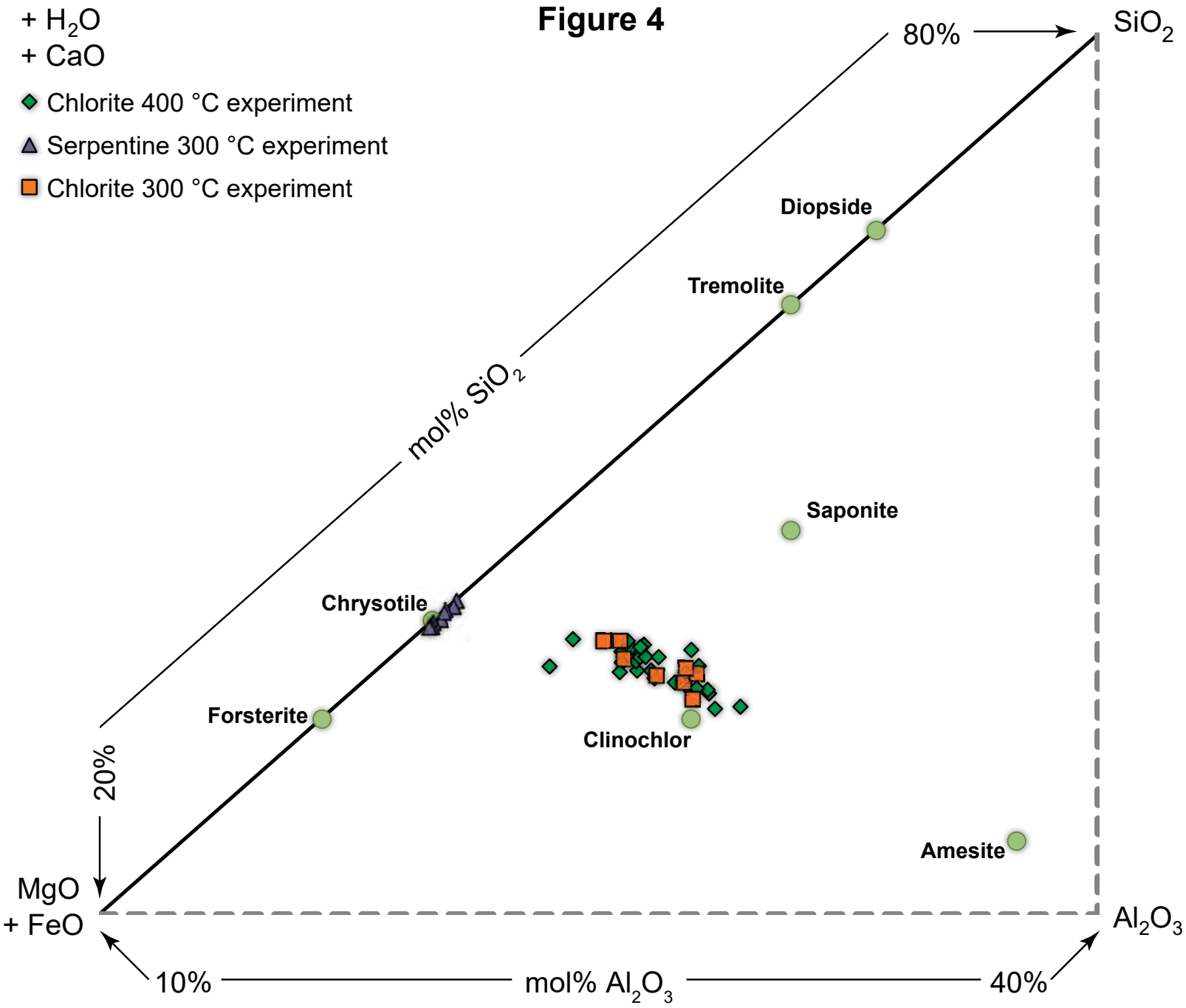
+ H_2O
+ CaO
Chlorite 400 °C experiment
Serpentine 300 °C experiment
Chlorite 300 °C experiment
Figure 4
80%
SiO_2
Diopside
Tremolite
mol% SiO_2
Saponite
Chrysotile
Forsterite
Clinochlor
Amesite
20%
MgO
+ FeO
Al_2O_3
10%
mol% Al_2O_3
40%

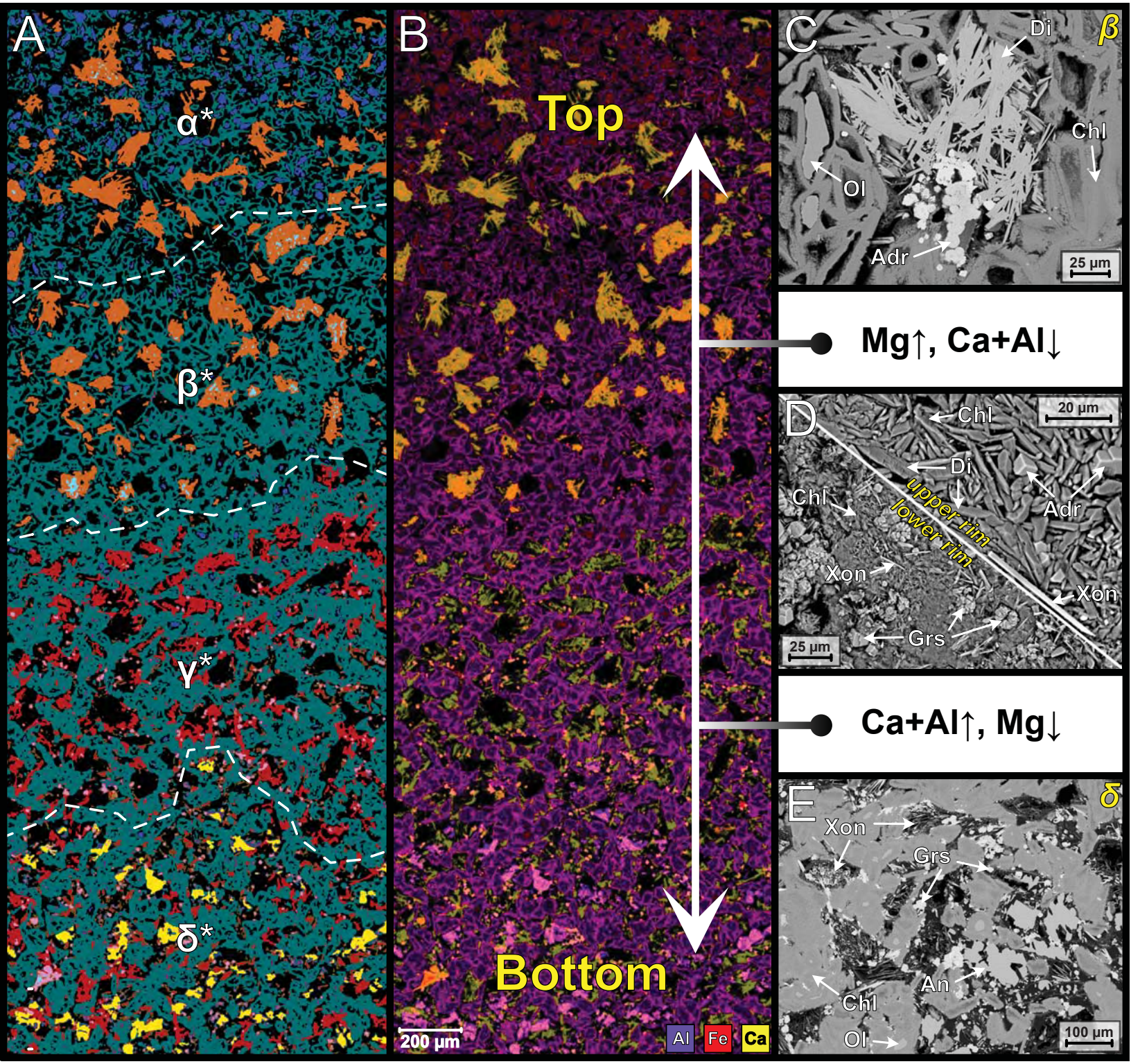
A
α*
β*
γ*
δ*
B
Top
Bottom
200 μm
Al
Fe
Ca
C
Di
β
Chl
Ol
Adr
25 μm
Mg↑, Ca+Al↓
D
Chl
20 μm
Di
Chl
upper rim
lower rim
Adr
Xon
Xon
Grs
25 μm
Ca+Al↑, Mg↓
E
δ
Xon
Grs
An
Chl
Ol
100 μm
Olivine
Plagioclase
Diopside
Xonotlite
Andradite
Grossular
Chlorite
Void

Figure 5

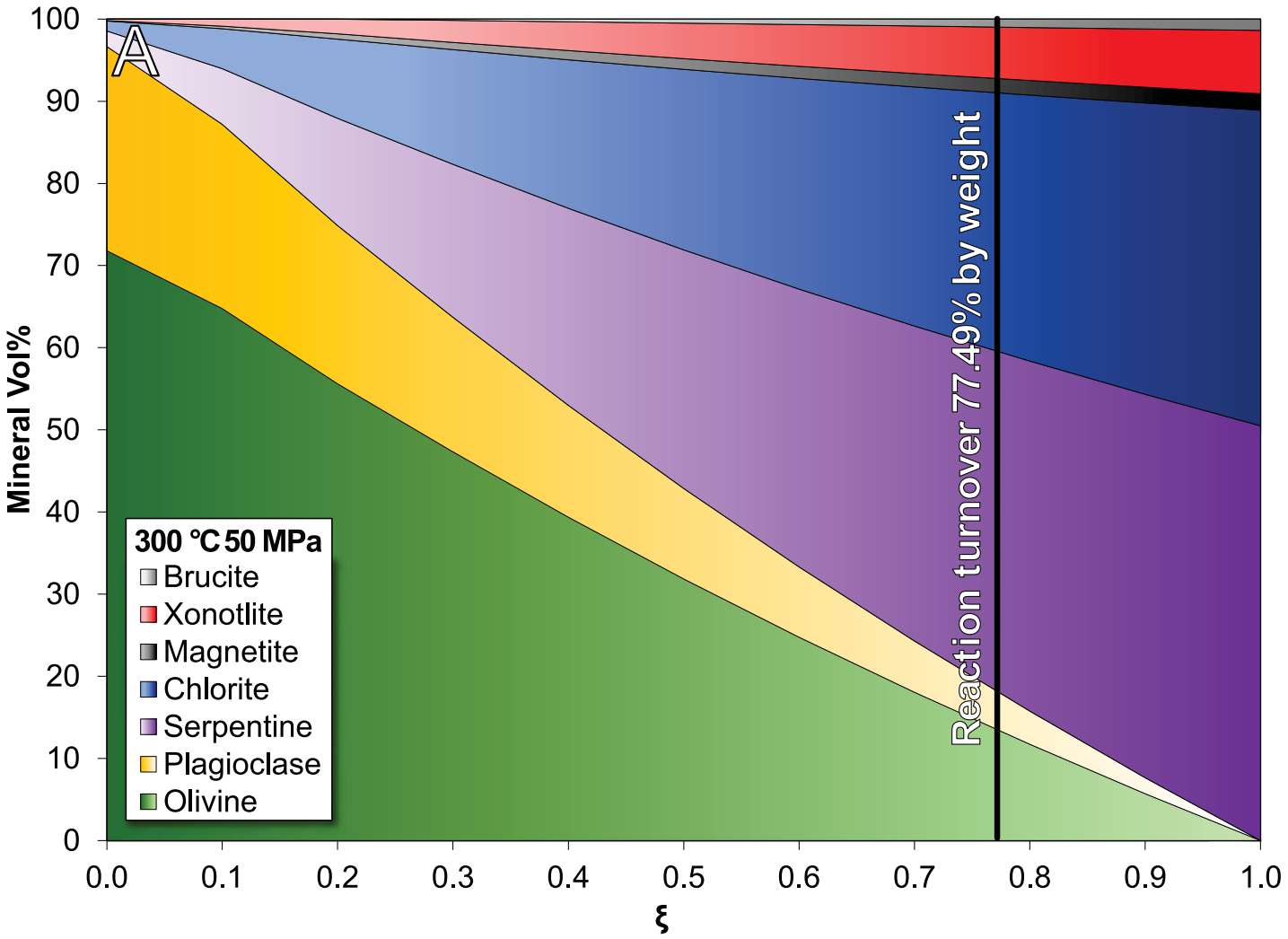
A
Mineral Vol%
ξ
300 °C 50 MPa
Brucite
Xonotlite
Magnetite
Chlorite
Serpentine
Plagioclase
Olivine
Reaction turnover 77.49% by weight

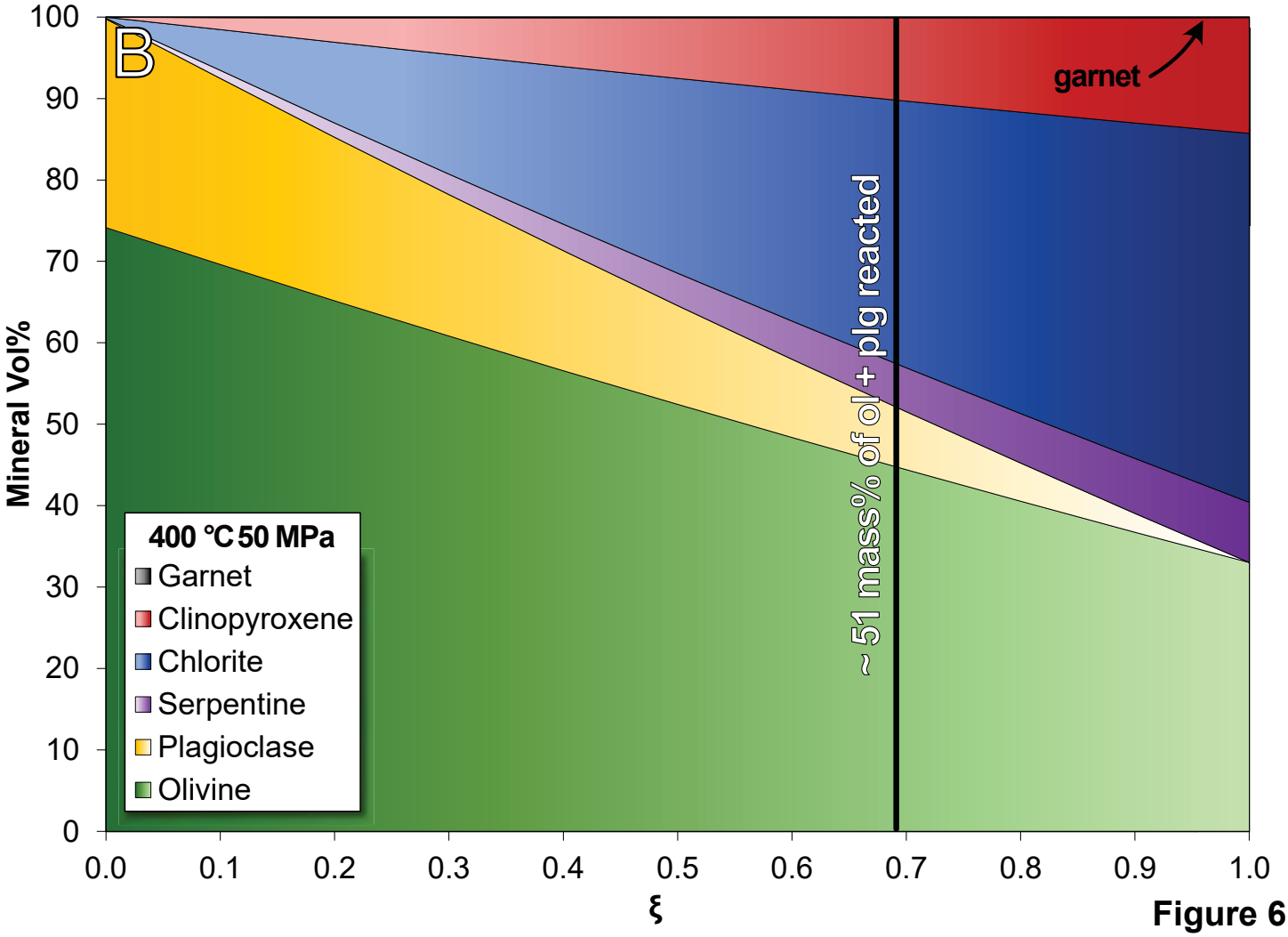
B
Mineral Vol%
ξ
400 °C 50 MPa
Garnet
Clinopyroxene
Chlorite
Serpentine
Plagioclase
Olivine
garnet
~ 51 mass% of ol + plg reacted

Figure 6

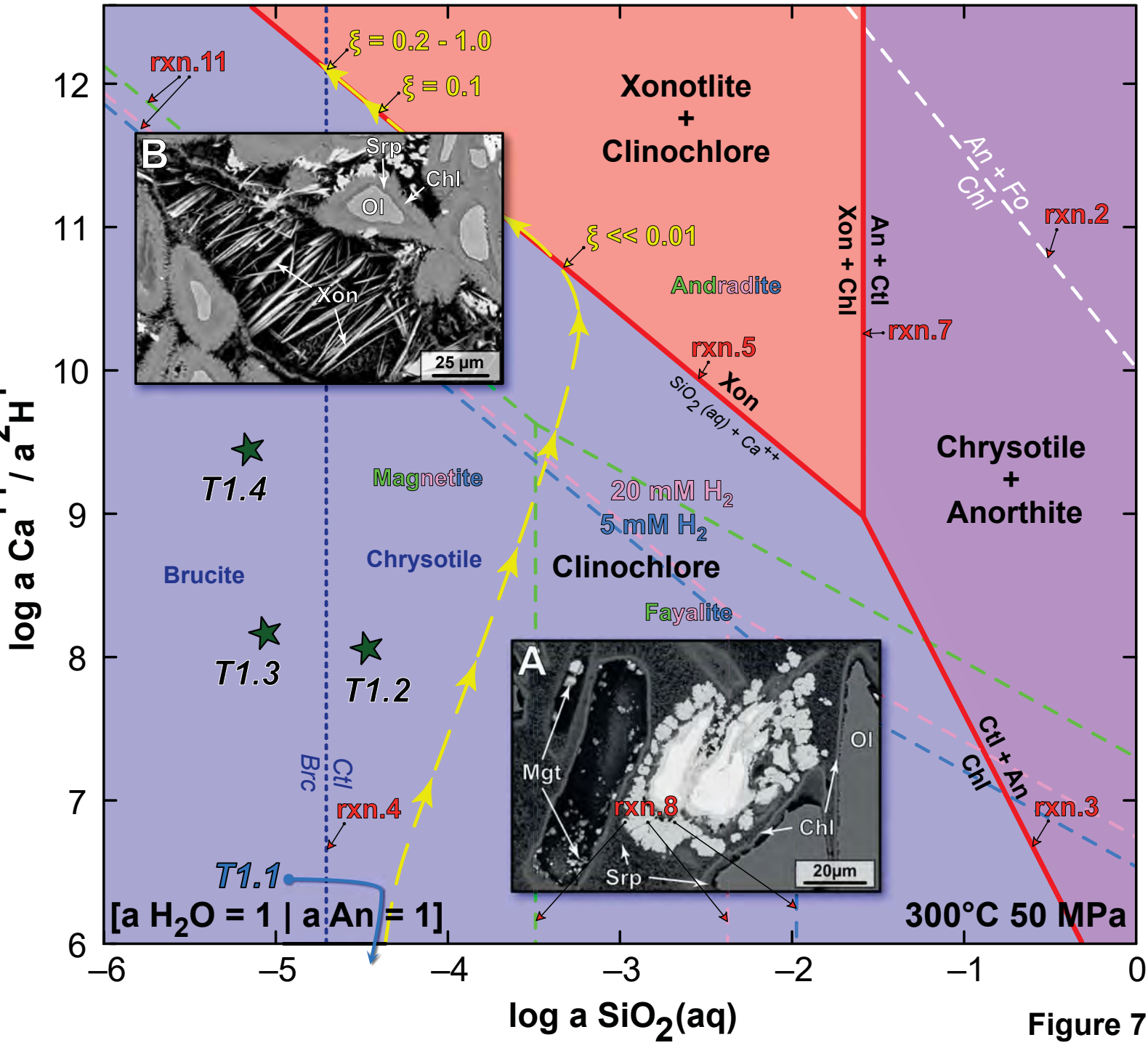
ξ = 0.2 - 1.0
ξ = 0.1
rxn.11
Xonotlite
+
Clinochlore
ξ << 0.01
Andradite
Xon + Chl
An + Ctl
An + Fo
Chl
rxn.2
rxn.7
rxn.5
Xon
SiO2 (aq) + Ca++
Chrysotile
+
Anorthite
Magnetite
20 mM H2
5 mM H2
Chrysotile
Clinochlore
Brucite
Fayalite
T1.4
T1.3
T1.2
T1.1
Ctl
Brc
rxn.4
Ctl + An
Chl
rxn.3
[a H2O = 1 | a An = 1]
300°C 50 MPa
B
Srp
Chl
Ol
Xon
25 µm
A
Mgt
Ol
rxn.8
Chl
Srp
20µm
log a Ca++ / a H+2
log a SiO2(aq)
12
11
10
9
8
7
6
–6
–5
–4
–3
–2
–1
0

Figure 7

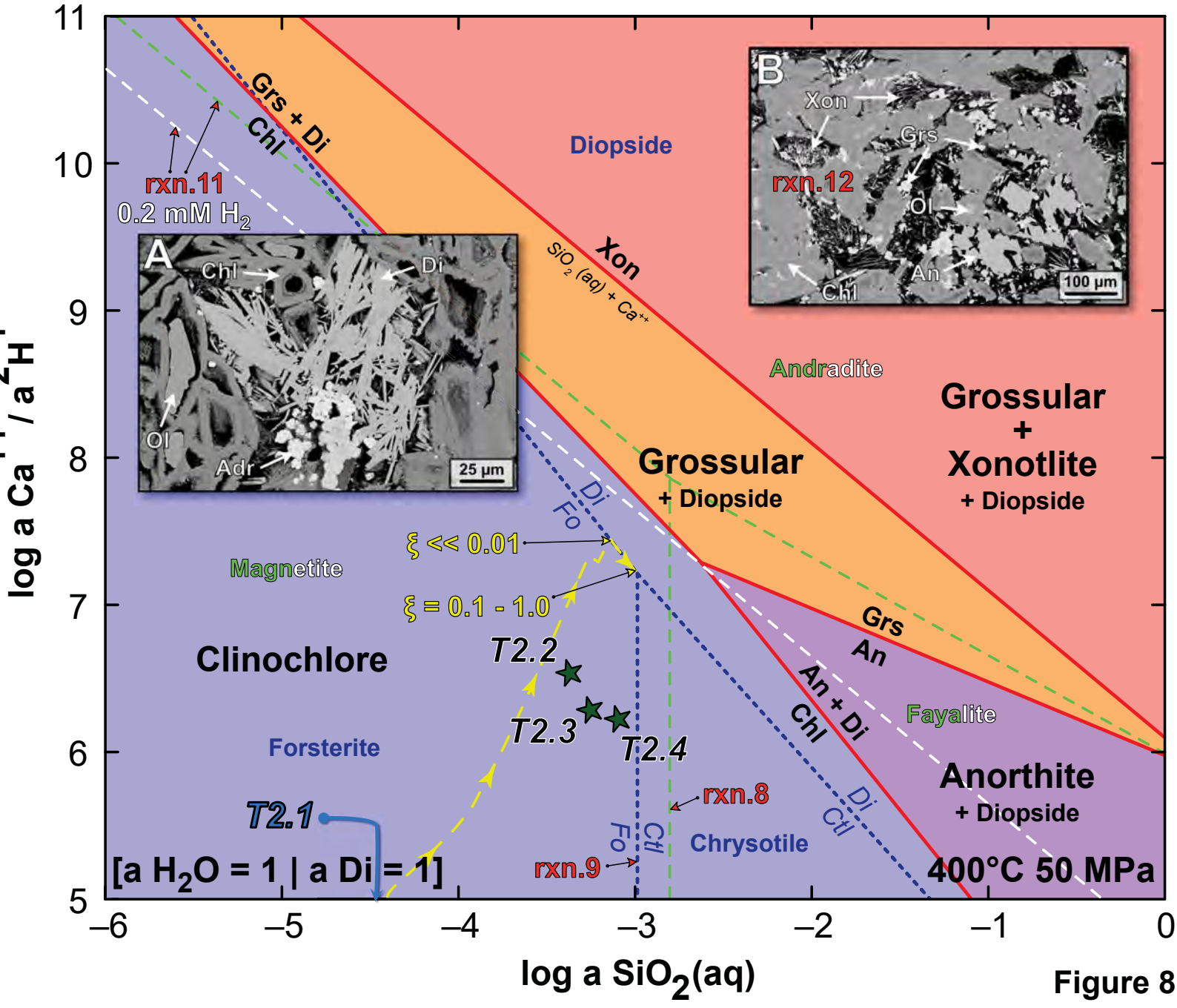
11
10
9
8
7
6
5
–6
–5
–4
–3
–2
–1
0
log a Ca++ / a 2H+
log a SiO2(aq)
Grs + Di
Chl
rxn.11
0.2 mM H2
Diopside
Xon
SiO2 (aq) + Ca++
Andradite
Grossular
+
Xonotlite
+ Diopside
Grossular
+ Diopside
Di
Fo
ξ << 0.01
ξ = 0.1 - 1.0
Magnetite
Clinochlore
T2.2
T2.3
T2.4
T2.1
Forsterite
[a H2O = 1 | a Di = 1]
rxn.8
rxn.9
Ctl
Fo
Chrysotile
Grs
An
An + Di
Chl
Fayalite
Anorthite
+ Diopside
Di
Ctl
400°C 50 MPa
A
Chl
Di
Ol
Adr
25 µm
B
Xon
Grs
rxn.12
Ol
Chl
An
100 µm

Figure 8